

Hard-constraint physics-residual networks enable robust extrapolation for hydrogen crossover prediction in PEM water electrolyzers

Yong-Woon Kim¹, Paul D. Yoo², Chan Yeob Yeun³,
Chulung Kang⁴, Yung-Cheol Byun^{5*}

¹Department of Computer Engineering, Regional Leading Research Center (RLRC), Jeju National University, Jeju, 63243, South Korea.

²Department of Computer Science and Information Systems, Birkbeck, University of London, London, UK.

³Centre for Cyber-Physical Systems, Department of Computer Science, Khalifa University, Abu Dhabi, 127788, UAE.

⁴Department of Mechanical System Engineering, Jeju National University, Jeju, 63243, South Korea.

⁵Department of Computer Engineering, Major of Electronic Engineering, Food Tech Center (FTC), Jeju National University, Jeju, 63243, South Korea.

*Corresponding author(s). E-mail(s): ycb@jejunu.ac.kr;
Contributing authors: ywkim@jejunu.ac.kr; p.yoo@bbk.ac.uk;
chan.yeun@ku.ac.ae; cukang@jejunu.ac.kr;

Abstract

Hydrogen crossover in polymer electrolyte membrane water electrolysis poses a critical safety and efficiency bottleneck for scalable green hydrogen production. While machine learning offers real-time monitoring capabilities, conventional data-driven neural networks (Pure NNs) and soft-constraint physics-informed neural networks (Standard PINNs) suffer from inherent optimization conflicts and fail catastrophically when extrapolating beyond sparse training conditions. Here, we present a hard-constraint physics-residual network (PR-Net) that embeds analytical transport equations—Henry’s law, Fick’s diffusion, and Faraday’s law—as a deterministic computational backbone, restricting the neural network to learn only systematic physical deviations. Across 184 experimental

points spanning six membrane types and operating conditions of 25–85°C, 1–200 bar, and 0.05–5.0 A cm⁻², this architecture intrinsically resolves gradient conflicts, yielding $R^2 = 99.57 \pm 0.16\%$ with a 39-fold reduction in training variance compared to purely data-driven models ($R^2 = 96.47 \pm 6.20\%$). Crucially, the PR-Net breaks the extrapolation barrier, maintaining $R^2 > 97\%$ at extreme cathode pressures up to 200 bar—a 2.5-fold extrapolation beyond the training domain where Standard PINN severely degrades ($R^2 = 72.2\%$) and Pure NN collapses ($R^2 = 58.7\%$). Furthermore, the learned residuals autonomously capture temperature-induced membrane swelling (Spearman’s $\rho = 0.506$, $p < 0.001$) and identify the non-linear transport regime transition near 0.23 A cm⁻², without explicit programming. Delivering millisecond-level inference on edge hardware, the PR-Net establishes a highly reliable, generalizable foundation for adaptive safety control and predictive maintenance in high-pressure electrochemical energy systems.

Keywords: Physics-residual network, Hard-constraint physics integration, Hydrogen crossover, PEM water electrolysis, Extrapolation robustness, Scientific machine learning, Deep ensemble uncertainty quantification

1 Introduction

Polymer electrolyte membrane (PEM) water electrolysis represents a cornerstone technology for green hydrogen production, offering rapid response times, high current densities, and compatibility with renewable energy sources[1–3]. However, hydrogen crossover through the membrane poses critical challenges to both operational safety and economic viability, with crossover rates approaching the explosive limit of 4 mol% H₂ in O₂ under certain operating conditions[4–6]. This phenomenon can reduce Faradaic efficiency and accelerate membrane degradation, increasing maintenance costs and downtime risk[5, 7, 8].

Current approaches to predict hydrogen crossover rely predominantly on physics-based models derived from Fick’s law and Henry’s law, requiring extensive calibration and computational resources that preclude real-time implementation[9–11]. While these models provide valuable mechanistic insights, they struggle with the complex, non-linear interactions between operating parameters, membrane properties, and degradation effects[12–14]. Recent advances in machine learning have demonstrated promising alternatives for electrochemical system modeling[15–17], yet purely data-driven approaches lack physical consistency and fail to extrapolate beyond training conditions—critical limitations for safety-critical applications[18, 19].

Physics-informed neural networks (PINN) offer a paradigm-shifting approach by seamlessly integrating physical laws as constraints within the neural network training process[19–21]. This hybrid methodology has shown remarkable success in fluid dynamics[22], heat transfer[23], and recently in PEM systems. For instance, recent temperature prediction PINNs for PEM electrolyzers reported improved accuracy compared with purely data-driven baselines[24]. Ko et al.[25] applied PINNs to remaining useful life prediction in PEM fuel cells, reporting improved data efficiency while

maintaining competitive accuracy. Polo-Molina et al.[26] developed the first PINN framework for membrane degradation modeling in PEM electrolyzers, successfully capturing long-term voltage evolution dynamics. Despite these advances demonstrating PINN’s capability in electrochemical systems, hydrogen crossover prediction has received comparatively limited attention in the PINN literature, to the best of our knowledge.

Beyond the question of application domain, a more fundamental methodological question remains unaddressed. While additive physics-residual decompositions have been explored in broader scientific machine learning contexts [27, 28], their application to electrochemical transport systems introduces distinct challenges: the physics backbone involves tightly coupled, nonlinear transport equations (Henry’s law, Fick’s diffusion, and Faraday’s law) rather than simple analytical priors, experimental data are inherently sparse ($n \approx 100\text{--}200$ points across diverse membrane types), and the safety-critical context demands quantified extrapolation guarantees under conditions that may significantly exceed the training domain. Whether hard-constraint residual architectures structurally outperform soft-constraint PINNs under these specific conditions—and by how much—remains undemonstrated.

Here, we present the first systematic application and comparison of three machine learning paradigms—purely data-driven neural networks (Pure NN), soft-constraint PINN (Standard PINN), and hard-constraint physics-residual networks (PR-Net)—for predicting hydrogen crossover in PEM water electrolyzers. To rigorously validate the universality of our proposed PR-Net, we deliberately eschewed single-lab experimental datasets, which are inherently prone to systematic equipment biases. Instead, we utilized an experimental dataset comprising 184 independent hydrogen crossover measurements compiled from eight peer-reviewed publications. Successfully learning across varying operational conditions, including temperatures of 25–85°C, cathode pressures of 1–200 bar, and current densities of 0.05–5.0 A cm⁻² across six membrane categories, demonstrates that the PR-Net captures fundamental transport physics rather than overfitting to lab-specific artifacts. By fundamentally shifting the learning objective from composite loss regularization to residual correction, we demonstrate that hard physics integration via residual learning systematically and substantially outperforms conventional data-driven and soft-constraint approaches in both accuracy and extrapolation robustness.

Specifically, our proposed PR-Net framework overcomes the critical bottlenecks of electrochemical machine learning through the following key advances. **First, it breaks the extrapolation barrier.** The PR-Net maintains unprecedented predictive accuracy ($R^2 > 97\%$) even at extreme cathode pressures up to 200 bar—representing a 2.5-fold extrapolation beyond the training domain—while Standard PINN degrades to $R^2 = 72.2\%$ and Pure NN collapse to $R^2 = 58.7\%$, exhibiting unphysical saturation behavior inconsistent with Henry’s law. **Second, it resolves inherent optimization conflicts.** By embedding analytical transport laws as a deterministic computational backbone, the architecture eliminates the gradient “tug-of-war” between data fidelity and physical compliance inherent in Standard PINN, yielding a 39-fold reduction in training variance ($CV_{R^2} = 0.16\%$ versus 6.20% for Pure NN) and ensuring reproducible model behavior essential for safety-critical deployment. **Furthermore, it**

enables autonomous mechanistic discovery. Without explicit programming, the learned residual corrections autonomously reveal temperature-induced membrane swelling as a systematic transport resistance (Spearman’s $\rho = 0.506$, $p < 0.001$) and accurately identify the critical transition from Fickian diffusion-dominated to Faraday production-dominated crossover near 0.23 A cm^{-2} , confirming that the underlying transport physics is intrinsically encoded in the residual representation. **Finally, it ensures real-time edge deployment capability.** With millisecond-level inference times and a compact architecture (34,305 parameters), the PR-Net enables safety-critical monitoring across hardware platforms ranging from a desktop PC to resource-constrained embedded devices (Raspberry Pi 5, $1.08 \pm 0.34 \text{ ms}$), satisfying the response-time requirements of industrial process control systems.

Together, these advances establish the PR-Net framework as a scalable foundation for adaptive safety monitoring and predictive maintenance in gigawatt-scale hydrogen production facilities, and offer a generalizable paradigm for hybrid physics-machine learning modeling in electrochemical energy systems where mechanistic transport models exist but require data-driven refinement.

2 Results

2.1 Hard versus soft physics integration: Systematic methodology comparison

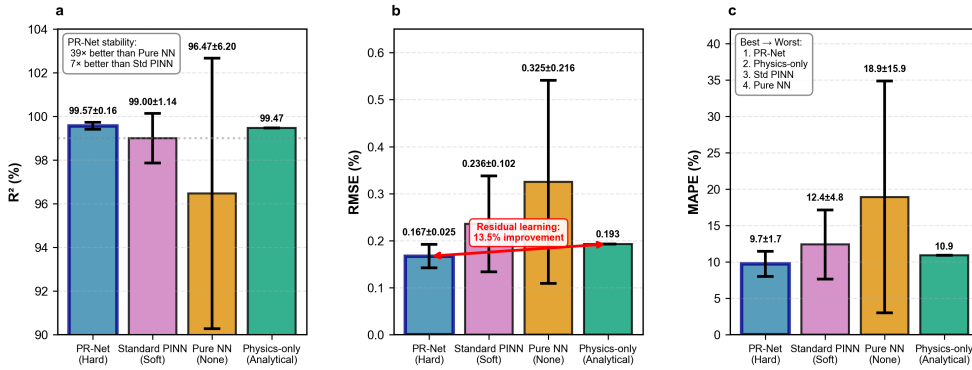


Fig. 1 Performance comparison of physics integration strategies for hydrogen crossover prediction. Metrics represent the mean \pm s.d. derived from 5-fold cross-validation repeated 20 times ($n = 100$ independent model instances per architecture). **a** Coefficient of determination (R^2). PR-Net demonstrates exceptional training stability, exhibiting a 39-fold reduction in variance compared to the purely data-driven model (Pure NN). **b** Root-mean-square error (RMSE) comparison. The residual learning framework achieves a 13% improvement in accuracy over the analytical physics-only baseline. **c** Mean absolute percentage error (MAPE) evaluation, highlighting the superior accuracy and robustness of the PR-Net architecture. All models were trained on 184 experimental data points for 700 epochs.

To rigorously evaluate the impact of physics integration strategies on predictive performance and training stability, we systematically compared our proposed PR-Net against two conventional paradigms: the purely data-driven Pure NN and Standard PINN utilizing soft constraints (Figure 1). All models were trained on identical 184 experimental data points for 700 epochs using stratified 5-fold cross-validation repeated 20 times, yielding 100 independent model instances per method to ensure robust statistical assessment.

Figure 1 demonstrates that PR-Net achieves superior performance across all metrics with exceptional stability. The coefficient of determination ($R^2 = 99.57 \pm 0.16\%$) exhibits 39-fold lower variance compared to Pure NN ($R^2 = 96.47 \pm 6.20\%$) and 7-fold improvement over Standard PINN ($R^2 = 99.00 \pm 1.14\%$). Notably, the physics-only model achieves $R^2 = 99.47\%$ with $\text{RMSE} = 0.193\%$, while PR-Net further reduces RMSE to 0.167% (13% improvement), confirming that the residual neural network successfully identifies and corrects systematic deviations in the analytical transport equations.

The performance disparity stems from fundamental differences in optimization landscape complexity. The **Standard PINN (soft-constraint)** optimizes a composite loss function:

$$\mathcal{L}_{total} = (1 - \beta)\mathcal{L}_{data} + \beta\mathcal{L}_{physics} \quad (1)$$

where the network directly predicts hydrogen concentration (\hat{y}_{NN}). This formulation forces gradient descent to navigate conflicting objectives, balancing data fitting against physical compliance. Our results indicate this ‘‘tug-of-war’’ leads to suboptimal convergence and substantial instability ($\text{CV}_{R^2} = 1.14\%$), as documented in recent PINN literature [1, 19, 21].

In contrast, the proposed **PR-Net (hard constraint)** utilizes a constitutive physics model as a deterministic backbone, with the neural network learning only the discrepancy (residual) between theoretical predictions and experimental observations. The architecture fundamentally simplifies the learning problem through structured prediction:

$$\hat{y}_{final}(x) = \Phi_{H_2}^{Phys}(x) + \text{NN}_{residual}(x) \quad (2)$$

where $\Phi_{H_2}^{Phys}(x)$ represents the theoretical hydrogen concentration derived from Henry’s law, Fick’s diffusion, and Faraday’s law [6, 29], and $\text{NN}_{residual}(x)$ captures the complex non-linear deviations arising from membrane swelling, variable tortuosity, and interfacial phenomena not fully accounted for in simplified transport equations. The loss function depends solely on final prediction error $\mathcal{L} = \text{MSE}(\hat{y}_{final}, y_{true})$, and the neural network is tasked with the simpler objective of learning systematic model errors rather than the full input-output mapping [4, 6]. By constraining the hypothesis space to residuals, PR-Net achieves superior convergence ($\text{CV}_{R^2} = 0.16\%$) and eliminates the optimization conflicts inherent in Standard PINN methods.

2.2 Breaking the Extrapolation Barrier: Robustness at 200 bar

Ideally, a safety monitoring model must provide reliable predictions even when operating conditions deviate significantly from historical data, such as during pressure

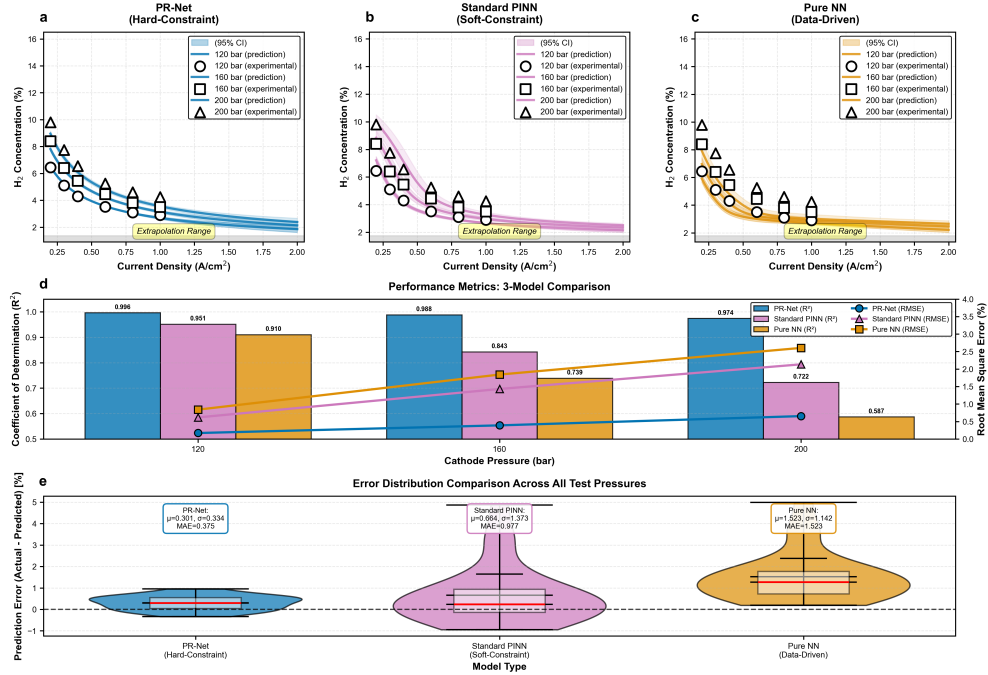


Fig. 2 Extrapolation robustness at extreme pressures beyond the training domain. a–c Comparative extrapolation performance of three modeling architectures. Models were trained on experimental data ≤ 80 bar and evaluated at unseen high-pressure regimes (120, 160, and 200 bar). **a** The PR-Net (hard-constraint) model maintains tight adherence to experimental measurements (symbols) with narrow 95% confidence intervals (shaded regions). **b, c** In contrast, the Standard PINN (soft-constraint) (**b**) and Pure NN (data-driven) (**c**) exhibit progressive deviation and increased uncertainty. **d** Quantitative performance degradation analysis. While all models perform comparably at 120 bar, a significant performance gap emerges at 200 bar. The PR-Net maintains an R^2 of 0.974, dramatically outperforming the Standard PINN ($R^2 = 0.722$) and Pure NN ($R^2 = 0.587$) approaches. **e** Error distribution analysis across all extrapolation pressures. Violin plots reveal that the PR-Net achieves a near-zero centered error distribution (mean $\mu = 0.301\%$), whereas alternative methods suffer from significant systematic bias ($\mu = 0.664\%$ for Standard PINN) and variance, confirming the stabilizing effect of the hard-constraint physics backbone.

surges or emergency shutdowns. To evaluate this critical capability, we subjected the trained models (on data ≤ 80 bar with 42 experiment points) to a stringent stress test at pressures of 120, 160, and 200 bar—representing a **2.5-fold extrapolation** beyond the training domain. To rigorously evaluate the models’ extrapolation capabilities, we employed a highly controlled train-test split strategy. While our overall training dataset integrates heterogeneous multi-lab data to ensure generalizability, the specific high-pressure extrapolation test was strictly isolated to data from a single experimental setup (Wu et al., 2025) [29].

Specifically, the models were trained on observations ≤ 80 bar (including the ≤ 80 bar subset from Wu et al.) and tested strictly on unseen high-pressure regimes (120–200 bar) from the same study. This deliberate design completely isolates the effect

of pressure domain shift from inter-laboratory measurement variances. By holding the experimental provenance constant, we unambiguously demonstrate that the catastrophic failure of Standard PINNs and Pure NNs at 200 bar is fundamentally due to their architectural inability to extrapolate thermodynamic laws, whereas the PR-Net robustly maintains physical consistency.

Figure 2 demonstrates the structural superiority of the PR-Net. As shown in Figure 2a, our proposed model strictly adheres to the thermodynamic trends predicted by Henry’s law, maintaining high accuracy ($R^2 > 97\%$) even at 200 bar. In sharp contrast, the Standard PINN (Figure 2b), despite including physics in its loss function, fails to generalize effectively. By 200 bar, its predictive power degrades significantly ($R^2 = 72.2\%$), exhibiting a “forgetting” phenomenon where the network prioritizes fitting training data over adhering to physical laws in the extrapolation regime. The Pure NN (Figure 2c) suffers degrades substantially ($R^2 = 58.7\%$), predicting physically implausible plateaus.

The quantitative impact of the physics backbone is highlighted in Figure 2d. While the performance gap is marginal at 120 bar, it widens progressively with increasing pressure. At the extreme 200 bar condition, the PR-Net reduces the RMSE by **68%** compared to the Pure NN and **35%** compared to the Standard PINN. Furthermore, the error distribution analysis (Figure 2e) reveals that our approach eliminates systematic bias ($\mu \approx 0.3\%$), whereas the Standard PINN exhibits a broad, heavy-tailed error distribution ($\sigma = 1.373$), indicating low confidence and reliability for safety-critical decision making. These results confirm that embedding physics as a computational backbone, rather than a soft regularization term, is the effective strategy for ensuring robustness in high-pressure hydrogen systems.

Statistical analysis corroborated these findings across all extrapolation pressures ($n = 24$). The Friedman omnibus test confirmed globally significant performance differences among the three architectures ($\chi^2 = 35.58$, $p < 0.001$). Post-hoc Wilcoxon signed-rank tests with Holm–Bonferroni correction demonstrated that the PR-Net significantly outperformed both Standard PINN ($r = -0.873$, $p_{\text{adj}} < 0.0001$) and Pure NN ($r = -0.993$, $p_{\text{adj}} < 0.0001$), with all effect sizes classified as large. Bootstrap confidence intervals confirmed that PR-Net reduced mean absolute error (MAE) by 0.726% relative to Standard PINN [95% CI: 0.376, 1.165] and by 1.149% relative to Pure NN [95% CI: 0.777, 1.588]. The PR-Net MAE degradation slope (0.0061%/bar) was 2.78 \times and 3.31 \times lower than that of Standard PINN and Pure NN, respectively, quantifying the accelerating performance divergence with extrapolation distance (Supplementary Table S12). Standard PINN likewise significantly outperformed Pure NN ($r = -0.993$, $p_{\text{adj}} < 0.0001$), confirming that even partial physics integration confers measurable benefit over purely data-driven approaches.

2.3 PR-Net achieves superior interpolation accuracy with enhanced stability

A critical challenge in applying machine learning to electrochemical systems is achieving high accuracy without overfitting, particularly when experimental data is scarce ($n = 184$, across diverse operating conditions such as 0.05 – 5.0 A cm⁻², 1-200 bar, 25 – 85°C). To rigorously evaluate the interpolation capability and training stability of

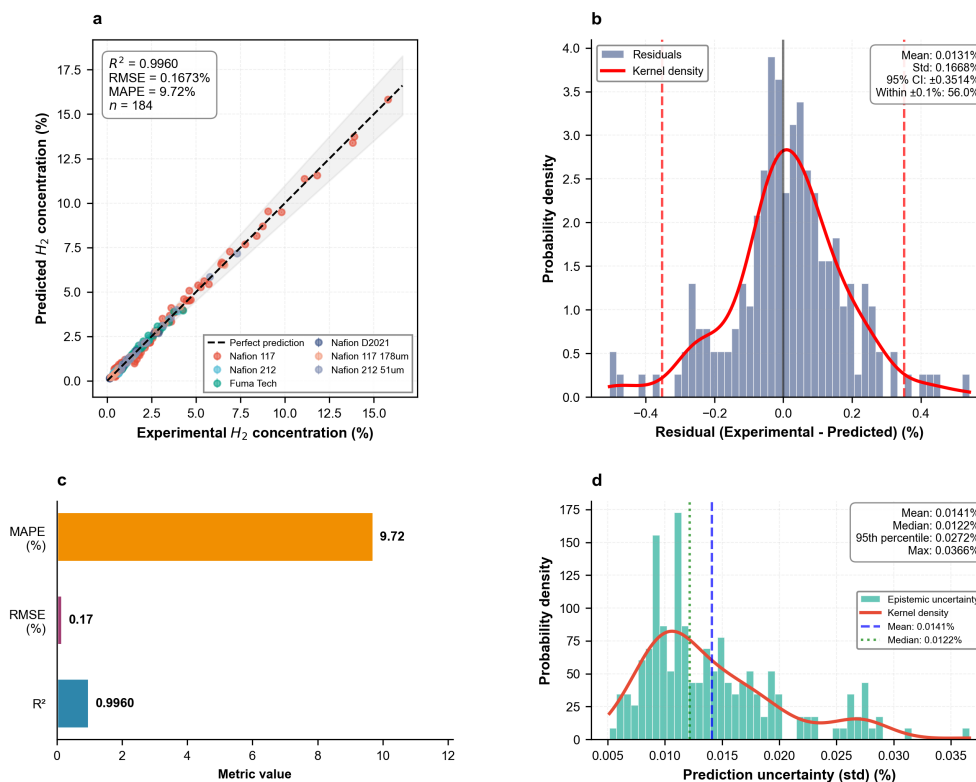


Fig. 3 High-precision interpolation and training stability on sparse experimental data. **a** Ensemble parity plot comparing predicted vs. experimental hydrogen crossover concentrations ($n = 184$). The PR-Net achieves an aggregate $R^2 = 0.9960$ and $\text{RMSE} = 0.1673\%$ using out-of-fold (OOF) predictions derived from 100 independent training runs (5-fold cross-validation \times 20 repetitions), demonstrating robust generalization despite the limited dataset size. **b** Residual distribution analysis showing unbiased predictions with a near-zero mean error (0.0131%) and Gaussian behavior (red curve), confirming the absence of systematic drift. **c** Summary of key performance metrics (MAPE, RMSE, R^2) highlighting the precision of the PR-Net. **d** Distribution of epistemic uncertainty (prediction standard deviation across the ensemble). The low mean uncertainty (0.0141%) indicates high model confidence and reproducible training dynamics, validated against the 95th percentile threshold (0.0272%).

the PR-Net, we employed a comprehensive validation protocol consisting of repeated 5-fold cross-validation (20 independent runs, totaling 100 trained models).

Figure 3 summarizes the aggregated out-of-fold (OOF) performance, representing the model’s generalized capability on unseen data. As shown in Figure 3a, the model achieves exceptional precision with an aggregate R^2 of **0.9960** and an RMSE of **0.1673%**, effectively capturing the diverse crossover behaviors across six different membrane types and varying operating conditions. This performance marginally exceeds the mean cross-validation score ($R^2 = 99.57\% \pm 0.16\%$), confirming that the aggregated ensemble prediction offers superior robustness compared to individual models.

Beyond point accuracy, the stochastic stability of the training process is a key indicator of reliability. The residual analysis (Figure 3b) reveals a strictly normal distribution centered at 0.0131%, indicating that the physics backbone successfully eliminated systematic bias. Furthermore, the analysis of epistemic uncertainty (Figure 3d) demonstrates the high reproducibility of our approach. The standard deviation of predictions across the ensemble is extremely low (mean $\sigma = 0.0141\%$), with 95% of predictions exhibiting uncertainty below 0.0272%. This tight confidence bound confirms that the physics-residual constraint effectively regularizes the optimization landscape, preventing the high-variance solutions typically observed in pure neural networks trained on small datasets.

2.4 Mechanistic Insights and Interpretability

Figure 4a deconstructs the inference mechanism, revealing that the neural network component ($\text{NN}_{\text{residual}}$) primarily applies negative corrections (Δy_{NN}) to the physics backbone (Φ_{phys}). This implies that theoretical models based on idealized parameters tend to systematically overestimate hydrogen crossover, a deviation autonomously corrected by our architecture. Crucially, the physics backbone enforces thermodynamic consistency in unobserved regimes. As shown in Figure 4b, the model strictly adheres to Henry’s law up to 200 bar, avoiding the unphysical saturation observed in pure data-driven approaches.

We further leveraged the residual network as a tool for scientific discovery. The distribution of learned residuals (Figure 4c) exhibits a statistically significant positive correlation with temperature (Spearman’s $\rho = 0.506$, $p < 0.001$). At standard operating temperatures (80–85°C), the residuals approach zero, indicating that the baseline physics model accurately captures the dominant transport phenomena. However, at lower temperatures (25°C), the network applies a significant negative correction. This pattern reveals that the idealized constitutive equations, which typically rely on Arrhenius-type temperature dependencies, systematically overestimate crossover at low temperatures. The network autonomously compensates for complex, unmodeled low-temperature phenomena, which may include contributions from reduced polymer chain mobility, increased water viscosity, and sluggish bubble detachment in the porous transport layers [6, 30]—effects that are difficult to incorporate into simplified constitutive equations. The consistency of this correction pattern across all six membrane types—spanning thicknesses of 51–260 μm and distinct ionomer structures including PFSA-based Nafion variants and FumaTech—suggests that the residual representation generalizes beyond membrane-specific artifacts without explicit programming.

Furthermore, the model correctly identifies the non-linear transition between transport regimes (Figure 4d). It detects the inflection point near 0.23 A cm^{-2} where the system shifts from diffusion-dominated (slope ≈ -0.13) to production-dominated transport (slope ≈ -0.40), confirming that the interplay between Fickian diffusion and Faraday’s law is successfully captured by the physics-residual framework.

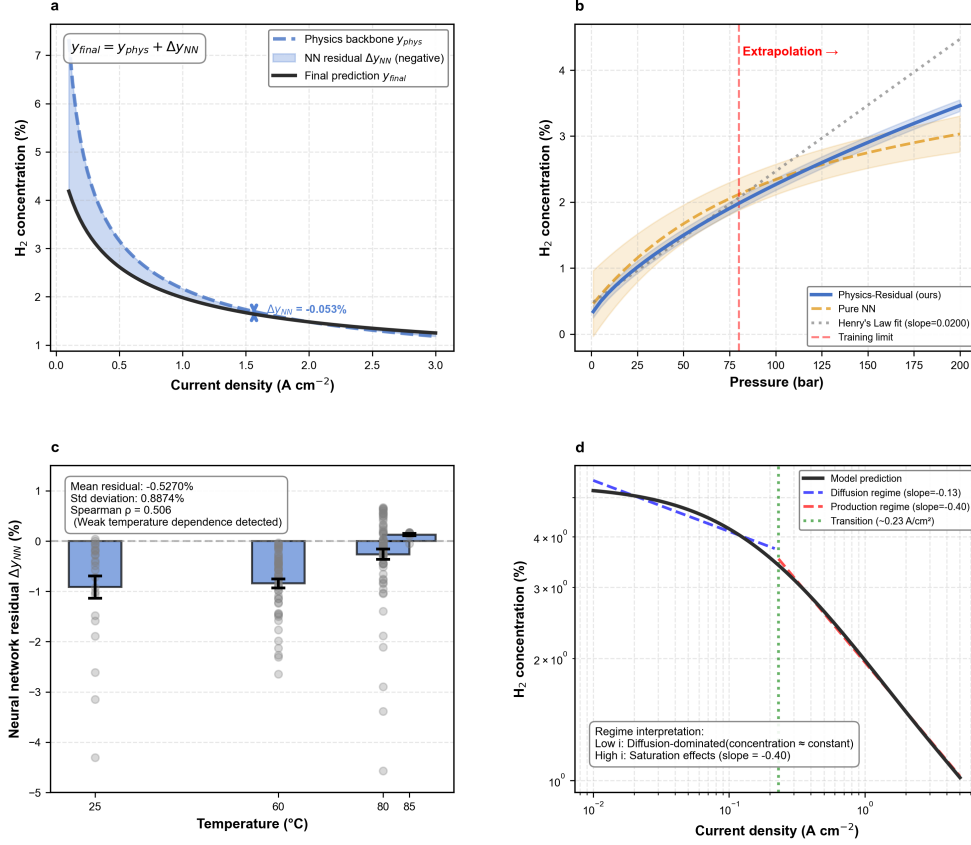


Fig. 4 Mechanistic interpretation and physical consistency of the PR-Net. **a** Decomposition of the prediction mechanism (80°C, 20 bar). The final prediction (black line) combines the physics backbone (blue dashed, Φ_{phys}) with a neural network residual correction (blue shaded, Δy_{NN}). The negative residual indicates the network compensates for systematic overestimation by the theoretical model. **b** Adherence to Henry’s law during extrapolation. The PR-Net (blue) maintains linear pressure-solubility consistency up to 200 bar, whereas the Pure NN (orange) exhibits unphysical saturation beyond the training limit (80 bar). **c** Physical interpretation of learned residuals. Neural network residuals (Δy_{NN}) show a statistically significant positive correlation with temperature (Spearman’s $\rho = 0.506$, $p < 0.001$), consistent with membrane swelling-induced transport resistance. Bars represent mean \pm s.d. **d** Capture of transport mechanism transition. The model identifies a regime shift from diffusion-dominated (slope ≈ -0.13) to production-dominated transport (slope ≈ -0.40) near 0.23 A cm $^{-2}$.

2.5 Uncertainty quantification and sensitivity analysis

Reliable uncertainty estimates are essential for risk assessment in safety-critical applications. We employed deep ensemble methods with 100 independent model trainings to quantify prediction uncertainty. The ensemble approach, trained on 42 experimental

data points, demonstrated well-calibrated confidence intervals, with 94.6% of experimental observations falling within the predicted 95% confidence bounds, indicating robust uncertainty quantification without overconfidence.

Sensitivity analysis revealed that current density exerts the dominant influence on hydrogen crossover ($2.94 \pm 5.98\%/(\text{A cm}^{-2})$), with the high standard deviation reflecting condition-dependent effects. Pressure showed moderate sensitivity ($0.066 \pm 0.055\%/bar$), while temperature ($0.020 \pm 0.027\%/^{\circ}\text{C}$) and membrane thickness ($0.013 \pm 0.023\%/μ\text{m}$) exhibited comparatively minor influences. The relatively weak temperature dependence aligns with the known characteristics of hydrogen solubility in polymer membranes [31]. The pronounced sensitivity to current density, coupled with its high variability, underscores the critical importance of precise current control for maintaining hydrogen purity in industrial PEM electrolyzers. These quantitative insights directly inform sensor placement priorities and measurement frequency requirements for industrial implementation.

2.6 Real-time deployment capability across hardware platforms

Critical to industrial implementation is the ability to deploy models on diverse hardware platforms for real-time monitoring and control. We benchmarked inference performance across three representative platforms: desktop PC (Intel-i7 RTX-4060 GPU), edge GPU (NVIDIA Jetson AGX Orin), and edge CPU (Raspberry Pi 5). All platforms achieved millisecond-level inference, remaining well below the 2 ms threshold required for integration into advanced process control systems.

The compact model size (34,305 parameters) enables deployment even on resource-constrained edge devices, facilitating distributed monitoring architectures essential for large-scale electrolyzer installations. The Raspberry Pi 5, representing the lower bound of computational capability, achieved mean inference times of 1.08 ± 0.34 ms, still well within the requirements for safety monitoring applications where hydrogen detector response times are typically on the order of seconds to tens of seconds (e.g., ISO 26142 specifies $t_{90} \leq 30$ s)[32, 33].

2.7 Economic impact and safety enhancement

The economic implications of accurate crossover prediction extend beyond efficiency improvements. Our analysis indicates potential annual savings of \$200,000–1,500,000 per facility through optimized maintenance scheduling and reduced unplanned downtime. Stack lifetime extension of 15–25% defers capital expenditures of \$100,000–500,000 per replacement cycle. Most critically, maintaining hydrogen concentration below the 4 mol% safety threshold prevents catastrophic failures, with 40% of hydrogen-related incidents attributed to undetected leaks[34].

The real-time monitoring capability enables adaptive control strategies that optimize the trade-off between production rate and membrane degradation. During periods of high renewable energy availability, operators can safely push current densities closer to limits while maintaining safety margins through continuous crossover monitoring. This dynamic optimization could improve overall system efficiency by 3–7%, significant given that electricity costs constitute 60–80% of hydrogen production expenses[35].

3 Discussion

This work reveals a fundamental insight for physics-informed machine learning: embedding physics as a deterministic computational backbone (PR-Net) fundamentally outperforms soft-constraint integration (Standard PINN) for both interpolation and extrapolation tasks. By shifting the learning paradigm from “regularization via loss functions” to “correction via residual learning,” the proposed PR-Net architecture achieves simultaneous excellence in accuracy, generalization, and training stability. The Standard PINN faces an inherent tension: minimizing data loss encourages fitting training points exactly, while minimizing physics loss encourages conforming to potentially imperfect physical models [17]. This compromise manifests as reduced interpolation accuracy (R^2 : 99.00% vs. 99.57%), extrapolation failure (R^2 : 72.2% vs. 97.4% at 200 bar), and high training variance (σ : 1.14% vs. 0.16%). The PR-Net resolves this tension by construction, ensuring that fundamental physical laws are guaranteed in every prediction rather than merely encouraged. This architectural robustness is particularly critical given the inherent heterogeneity of our training dataset; by anchoring predictions to a deterministic backbone, the model successfully distills universal physical trends while effectively filtering the inter-laboratory measurement noise and systematic biases present in aggregated literature data.

Crucially, the PR-Net transcends conventional predictive modeling by serving as an autonomous tool for scientific discovery. The explicit decoupling of the physics baseline from the neural network residual enables the extraction of unmodeled physical phenomena that neither purely data-driven nor purely physics-based approaches can isolate independently. The network autonomously identified a statistically significant positive correlation between learned residuals and operating temperature (Spearman’s $\rho = 0.506$, $p < 0.001$), providing data-driven evidence that simplified Arrhenius-type constitutive equations systematically overestimate crossover at sub-ambient temperatures—a deviation consistent with unmodeled reductions in polymer chain mobility, elevated water viscosity, and sluggish bubble detachment in the porous transport layer. Notably, this correction pattern is consistent across all six membrane types spanning ionomer chemistries and thicknesses of 51–260 μm , suggesting that the residual encodes membrane-agnostic transport physics rather than membrane-specific artifacts. Furthermore, without explicit supervision, the model precisely captured the non-linear transition between transport regimes, identifying the inflection near 0.23 A cm^{-2} where the system shifts from diffusion-dominated to production-dominated transport (slopes ≈ -0.13 and -0.40 , respectively). This capacity to isolate and quantify unmodeled transport mechanics offers a new paradigm for refining theoretical electrochemical models.

The PR-Net’s ability to maintain $R^2 > 97\%$ at pressures $2.5\times$ beyond the training range provides reliability essential for safety-critical applications, as hydrogen crossover approaching 4 mol% H_2 in O_2 constitutes a severe explosion hazard [4]. However, we acknowledge that the physics backbone’s pressure dependence—governed by Henry’s law and the LGDL pressure-correction term (Eqs. 7 and 9)—assumes ideal gas behavior. At pressures approaching 200 bar, intermolecular interactions cause non-negligible deviations from ideality, and a fully rigorous treatment would incorporate fugacity corrections of the form $f_{\text{H}_2} = \phi(T, P) \cdot P$, where ϕ is the fugacity coefficient

from a real-gas equation of state such as the Peng–Robinson model [36]. It is noteworthy, however, that the residual network is structurally free to apply large corrections precisely where the backbone deviates most; the high accuracy observed at 200 bar therefore suggests that the residual component partially absorbs non-ideal contributions within the range tested, even absent explicit fugacity modeling. Future backbone extensions operating routinely above 150 bar should incorporate equation-of-state corrections to ensure thermodynamic self-consistency, without altering the fundamental PR-Net architecture.

A potential challenge often associated with meta-analytical datasets is the compounding of epistemic uncertainties arising from disparate experimental setups. However, our results demonstrate that the PR-Net uniquely leverages this diversity. By subjecting the architecture to a realistic distribution of operational variabilities across 184 independent observations, we provide a more rigorous stress-test of generalization than a tightly controlled single-lab dataset could offer. This establishes the PR-Net not just as a predictive tool, but as a robust framework for meta-learning in electrochemical systems where data is sparse and noise is multi-sourced.

From an industrial deployment perspective, the 39-fold variance reduction in training stability and the maintained millisecond-level inference time collectively establish the foundation for safety-critical real-time monitoring. By continuously tracking crossover concentration against set-points, adaptive control systems could modulate current density and pressure during renewable energy transients, enabling safe operation closer to efficiency limits. Prior techno-economic analyses indicate that energy costs constitute 60–80% of hydrogen production expenses [37], and that improvements in system-level efficiency on the order of several percentage points could represent substantial annual savings at MW-scale installations [38, 39]. Furthermore, stack replacement costs for PEM systems have been reported in the range of \$100,000–500,000 per cycle [38]; monitoring systems capable of reducing unplanned membrane failures and enabling targeted maintenance scheduling could therefore plausibly reduce a significant fraction of these costs, though the specific magnitude of savings depends on installation scale, maintenance baseline, and control architecture. We emphasize that these projections are derived from published cost benchmarks rather than direct model outputs, and their realization requires integration with closed-loop control systems validated under sustained dynamic conditions. In particular, the present model is trained on static experimental observations and does not incorporate time-series aging trajectories; quantitative lifetime extension projections must therefore await future work combining PR-Net’s real-time accuracy with dedicated time-resolved degradation datasets.

These findings have broad implications for physics-informed machine learning across scientific domains. Treating physics as a computational backbone and learning only residual corrections offers a principled approach that preserves the strengths of both physics-based and data-driven modeling [40]. This paradigm extends naturally to battery degradation modeling, fuel cell lifetime prediction [25], and other electrochemical systems where mechanistic transport equations exist but require data-driven refinement of unmodeled interfacial phenomena. As electrolyzer technology evolves toward higher pressures and temperatures, augmenting the physics backbone

with non-ideal thermodynamic corrections and transient degradation models will be essential to sustain the extrapolation robustness demonstrated here—ultimately supporting large-scale green hydrogen deployment aligned with long-term decarbonization targets [37].

4 Methods

4.1 Data collection and preprocessing

Dataset composition. This study utilizes an experimental dataset comprising 184 independent hydrogen crossover measurements compiled from eight peer-reviewed publications spanning 2011–2025, each corresponding to a distinct combination of operating conditions and membrane type. By consolidating data across eight independent experimental setups, this dataset captures a realistic distribution of epistemic uncertainties and operational variabilities inherent to industrial electrolyzer deployment. This design choice deliberately subjects the modeling architectures to a more rigorous, noisy, and generalized environment than a tightly controlled single-experiment dataset could provide, strictly stress-testing the models’ physical consistency. The dataset covers temperatures of 25–85°C, cathode pressures of 1–200 bar, and current densities of 0.05–5.0 A cm⁻², across six membrane categories, spanning operating ranges relevant to both laboratory-scale and industrial PEM electrolyzer conditions. This compilation provides a robust foundation for model training and validation without reliance on synthetic data augmentation.

Data sources and extraction. Experimental data were extracted from the following studies: Grigoriev et al. [41], Schalenbach et al. [5], Trinke et al. [4], Garbe et al. [42], Stähler et al. [43], Martin et al. [44], Bernt et al. [45], and the most recent work by Wu et al. [29]. For each study, the target variable (hydrogen concentration in the oxygen stream, %) and corresponding operating parameters (temperature, cathode pressure, current density, and membrane specifications) were simultaneously extracted to preserve the full multivariate structure of each experimental observation. Data extraction from published figures utilized WebPlotDigitizer (version 4.6) with manual verification against tabulated values where available. The estimated digitization uncertainty is below ±2% of the reported values. Each extracted data point was cross-referenced with reported experimental conditions to ensure accuracy. Anode pressure took one of two discrete values (1 bar or 5 bar); the atmospheric value (1 bar) was assumed when not explicitly reported, consistent with standard differential-pressure operation in PEM water electrolysis [1]. No imputation was performed for primary variables (temperature, cathode pressure, current density, and membrane thickness); data points with missing primary variables were excluded from the dataset.

Input features. Each data point included eight input parameters:

- Temperature: 25–85°C
- Cathode pressure: 1–200 bar
- Anode pressure: 1 or 5 bar (1 bar assumed when not explicitly reported)
- Membrane thickness: 51–260 μm
- Current density: 0.05–5.0 A cm⁻²

- Membrane type: categorical (one-hot encoded, 6 classes)
- Mechanical compression: 0–25 μm
- Platinum interlayer: categorical (binary; 0 = no interlayer, 1 = interlayer present)

The target variable was measured hydrogen concentration in the oxygen stream, ranging from 0.14% to 15.8%. The ranges above denote the span of experimental conditions represented in the compiled dataset.

Although platinum-interlayer membrane data are available in one of the compiled source studies [44], the present work deliberately restricts the training dataset to non-interlayer membranes (platinum interlayer position = 0 for all 184 observations) to ensure a homogeneous dataset structure and avoid confounding the physics-residual decomposition with an additional categorical transport mechanism at this stage. The platinum interlayer feature is nonetheless retained as an architectural input to maintain forward compatibility, as incorporation of platinum-interlayer data represents a natural and planned extension of this framework in future work.

Membrane types. Six membrane categories were represented: Nafion 117 (209 μm as reported in source studies, $n = 66$), Nafion 212 (58 μm , $n = 32$), Nafion D2021 (110 μm , $n = 21$), FumaTech E-730 (260 μm , $n = 28$), Nafion 117 (178 μm) ($n = 20$), and Nafion 212 (51 μm) ($n = 17$). Membrane types were encoded using one-hot encoding to preserve categorical distinctions without imposing ordinal relationships.

Data preprocessing. All continuous input features were normalized using min-max scaling to the range $[0, 1]$ to ensure balanced gradient propagation during training:

$$x_{\text{norm}} = \frac{x - x_{\min}}{x_{\max} - x_{\min}} \quad (3)$$

Scaling parameters were computed exclusively on the training set and applied consistently to validation and test sets to prevent data leakage.

Data split and validation. Two distinct validation protocols were employed depending on the evaluation objective.

Protocol 1 — Interpolation performance and training stability. To assess model accuracy and training stability within the experimental domain, stratified five-fold cross-validation was employed with stratification by membrane type to ensure balanced representation of all six membrane categories across folds. To account for stochastic initialization effects, each fold was repeated with 20 independent runs, yielding 100 trained model instances per architecture. This extensive sampling enables robust estimation of both mean performance and training variance, as reported in Section 2.3. Scaling parameters for input normalization were computed exclusively on each training fold and applied consistently to the corresponding validation fold to prevent data leakage.

Protocol 2 — Extrapolation capability and uncertainty quantification. To rigorously evaluate extrapolation performance beyond the training domain, a deep ensemble approach [46] consisting of 100 independently trained models was employed. These models were trained exclusively on data with cathode pressures ≤ 80 bar ($n = 42$)

to strictly isolate the high-pressure extrapolation regime (120, 160, and 200 bar) as a fully unseen test set. Each ensemble member was initialized with a sequential random seed (base seed 42 + model index, where model index ranges from 0 to 99) to ensure reproducibility while capturing epistemic uncertainty across the ensemble. Identical hyperparameter settings (700 epochs maximum, early stopping with patience of 150 epochs) were applied across both protocols to ensure consistency of comparison.

4.2 Neural network architecture

This study implements and compares two distinct physics integration strategies using identical neural network backbones to ensure fair comparison: the proposed PR-Net and the Standard PINN. Both methods share the same feedforward network structure, differing only in how physical knowledge is incorporated.

4.2.1 PR-Net Architecture (Proposed Method)

The PR-Net decomposes the prediction task into two complementary components:

$$\hat{y}_{final} = \Phi_{H_2}^{phys}(x) + NN_{residual}(x) \quad (4)$$

where $\Phi_{H_2}^{phys}(x)$ is the physics model prediction computed analytically (detailed in Section 4.3.1), and $NN_{residual}(x)$ is a neural network that learns the systematic residual between physics predictions and experimental observations.

The residual network employs a feedforward architecture with structure 8-128-128-128-1 (input \rightarrow hidden \rightarrow hidden \rightarrow hidden \rightarrow output) using tanh activation functions. The eight input neurons correspond to the normalized operating parameters (temperature, cathode pressure, anode pressure, membrane thickness, current density, membrane type encoding, compression, and platinum interlayer position), and the single output neuron produces the residual correction term. Unlike conventional neural networks that predict the target variable directly, this structural decomposition guarantees that the base prediction inherently respects established transport laws. The specific loss formulation and regularization strategy used to optimize this architecture are detailed in Section 4.3.3.

4.2.2 Standard PINN Architecture (Baseline Method)

For comparison, we implemented a conventional soft-constraint PINN that directly predicts hydrogen concentration while incorporating physics knowledge through a weighted loss function:

$$\hat{y}_{soft} = NN_{direct}(\mathbf{x}) \quad (5)$$

The network architecture is identical to the PR-Net (8 \rightarrow 128 \rightarrow 128 \rightarrow 128 \rightarrow 1 with tanh activation) to ensure fair comparison. The key difference lies in the training objective, which balances data fidelity and physics compliance through weighted loss terms (detailed in Section 4.3).

4.2.3 Shared Architectural Components

Network structure. Both architectures employ three hidden layers with 128 neurons each, yielding 34,305 total trainable parameters. This relatively shallow architecture was selected based on recent evidence that shallow PINN architectures can be effective for coupled multi-physics problems while offering stable training behavior [21, 47]. The tanh activation function was chosen following successful implementations in electrochemical system modeling, providing smooth gradients essential for physics constraint enforcement [19, 24].

Initialization. Network weights were initialized using Xavier uniform initialization [48] to maintain variance across layers:

$$W \sim \mathcal{U} \left(-\sqrt{\frac{6}{n_{in} + n_{out}}}, \sqrt{\frac{6}{n_{in} + n_{out}}} \right) \quad (6)$$

where n_{in} and n_{out} denote the number of input and output neurons for each layer. Biases were initialized to zero. This initialization strategy promotes stable gradient flow during early training epochs.

Architecture rationale. The compact three-layers architecture was chosen to balance model expressiveness with computational efficiency, particularly for edge deployment scenarios where memory and computational resources are constrained. Preliminary experiments with deeper architectures (4–5 hidden layers) showed no significant accuracy improvement while increasing inference time and training instability. The 128-neuron width provides sufficient capacity to capture complex nonlinear relationships while maintaining millisecond-level inference on all target hardware platforms.

4.3 Physics model and loss formulations

This section describes the physics model shared by both architectures and the distinct loss formulations that differentiate the physics-residual approach (PR-Net) from conventional soft-constraint (standard PINN) methods.

4.3.1 Physics Model (Shared Component)

The physics model $\Phi_{H_2}^{phys}$ calculates theoretical hydrogen crossover concentration based on established electrochemical transport equations. This model serves as the computational backbone in the PR-Net and as the soft-constraint target in the Standard PINN.

Gas Solubility and Pressure (Henry’s Law and Darcy’s Law). The hydrogen concentration at the membrane interface corresponds to the dissolved hydrogen concentration determined by Henry’s law:

$$c_{H_2}^* = S_{H_2}(T) \cdot P_{H_2}^{mem} \quad (7)$$

where $S_{H_2}(T)$ is the temperature-dependent solubility derived from the Bunsen coefficient:

$$\beta_{H_2} = \exp\left(-39.9611 + \frac{53.9381}{T/100} + 16.3135 \ln\left(\frac{T}{100}\right)\right) \quad (8)$$

The effective hydrogen pressure $P_{H_2}^{mem}$ at the catalyst layer interface accounts for the pressure drop through the liquid/gas diffusion layer (LGDL) using a correction factor K_D :

$$P_{H_2}^{mem} = \sqrt{P_{ca}^2 + K_D \cdot i} \quad (9)$$

Effective Diffusion (Fick's Law). Diffusive transport through the membrane is governed by Fick's law, adjusted for the membrane's water content (λ_m) and volume fraction. The hydrogen diffusion coefficient in water follows an Arrhenius relationship:

$$D_{H_2,w}(T) = 7.734 \times 10^{-6} \cdot \exp\left(-\frac{2225.4}{T}\right) \quad [\text{m}^2/\text{s}] \quad (10)$$

The effective diffusion coefficient incorporates membrane structural parameters:

$$D_{eff}^{H_2} = \frac{\varepsilon_{m,w}}{\tau_m} D_{H_2,w}(T) \quad (11)$$

where $\varepsilon_{m,w}$ is the water volume fraction calculated from membrane water content and equivalent weight, and $\tau_m = (1 - 0.85(1 - \varepsilon_{m,w}))^{-1}$ is the tortuosity factor.

Membrane-Specific Mass Transport Parameters. The mass transport coefficient $k_{MT} = \alpha \cdot i^\beta$ employs membrane-specific parameters derived from power law and logarithmic relationships:

$$\alpha = a_\alpha \cdot P^{b_\alpha} \cdot (1 + 0.005(T - 60)) \quad (12)$$

$$\beta = a_\beta + b_\beta \cdot \ln(P) \cdot (1 + 0.003(T - 60)) \quad (13)$$

where the coefficients ($a_\alpha, b_\alpha, a_\beta, b_\beta$) were optimized independently for each membrane type through nonlinear regression against experimental data.

Combined Mass Transport (Diffusion and Convection). The total hydrogen crossover flux $N_{H_2}^{co}$ incorporates both diffusive flux and convective/migration effects:

$$N_{H_2}^{co} = \frac{D_{eff}^{H_2} \cdot c_{H_2}^* + \frac{i}{2F}}{1 + \frac{k_{MT} \cdot t_{dif}}{D_{eff}^{H_2}}} \quad (14)$$

where t_{dif} is the total diffusion path length including the membrane and catalyst layers.

Final Hydrogen Concentration. The theoretical hydrogen concentration in the oxygen stream is derived from the ratio of hydrogen crossover flux to the total gas production rate predicted by Faraday's law:

$$\Phi_{H_2}^{phys} = \frac{N_{H_2}^{co}}{N_{O_2} + N_{H_2}^{co}} \times 100 \quad \text{where} \quad N_{O_2} = \frac{i}{4F} \quad (15)$$

This formulation maintains physical consistency across operating conditions spanning 0.05–5.0 A cm⁻², 1–200 bar, and 25–85°C. Detailed constitutive equations governing compression effects and additional transport phenomena are provided in Supplementary Methods.

4.3.2 Soft-Constraint Loss (Standard PINN Method)

The conventional soft-constraint approach enforces physics compliance through a weighted composite loss function:

$$\mathcal{L}_{soft} = (1 - \beta) \cdot \mathcal{L}_{data} + \beta \cdot \mathcal{L}_{physics} \quad (16)$$

where $\beta \in [0, 1]$ is the physics weight parameter that balances data fidelity and physics compliance. The data loss minimizes the mean squared error between network predictions and experimental measurements:

$$\mathcal{L}_{data} = \frac{1}{N} \sum_{k=1}^N \left(\hat{y}_{NN}^{(k)} - y_{true}^{(k)} \right)^2 \quad (17)$$

The physics loss acts as a soft constraint regularization term, penalizing deviations from the theoretical hydrogen crossover concentration:

$$\mathcal{L}_{physics} = \frac{1}{N} \sum_{k=1}^N \left(\hat{y}_{NN}^{(k)} - \Phi_{H_2}^{phys}(\mathbf{x}^{(k)}) \right)^2 \quad (18)$$

The physics weight β was systematically varied from 0.01 to 0.7 with adaptive scheduling (linear decay from 0.7 to 0.01 over training) through cross-validation. This approach represents the conventional paradigm where physics “regularizes” the neural network by encouraging—but not guaranteeing—physically consistent predictions.

Limitation. The soft-constraint formulation creates an inherent tension: the network must simultaneously minimize two potentially conflicting objectives. When the physics model has systematic errors (as all simplified models do), minimizing $\mathcal{L}_{physics}$ can degrade data fitting performance, while ignoring physics constraints compromises extrapolation capability.

4.3.3 Physics-Residual Loss (Proposed PR-Net Method)

The PR-Net approach embeds the physics model directly in the prediction architecture (as defined in Eq. 4) while employing a composite loss function that balances prediction accuracy with residual magnitude regularization:

$$\mathcal{L}_{total} = \mathcal{L}_{data} + \lambda \cdot \mathcal{L}_{residual} \quad (19)$$

The data loss \mathcal{L}_{data} ensures accurate prediction of experimental observations through the combined physics-residual output:

$$\mathcal{L}_{data} = \frac{1}{N} \sum_{k=1}^N \left(\hat{y}_{final}^{(k)} - y_{true}^{(k)} \right)^2 = \frac{1}{N} \sum_{k=1}^N \left(\Phi_{H_2}^{phys}(x^{(k)}) + NN_{residual}(x^{(k)}) - y_{true}^{(k)} \right)^2 \quad (20)$$

The residual loss ($\mathcal{L}_{residual}$) provides explicit L2 regularization on the magnitude of the learned neural network corrections, encouraging the model to rely primarily on

the physics backbone:

$$\mathcal{L}_{residual} = \frac{1}{N} \sum_{k=1}^N \left(NN_{residual}(x^{(k)}) \right)^2 \quad (21)$$

The regularization weight λ controls the trade-off between prediction accuracy and physics reliance. A larger λ constrains the residual network to output smaller corrections, forcing greater dependence on the physics model—beneficial for extrapolation where physics provides the primary predictive power. In this study, $\lambda = 2.0$ was selected based on cross-validation experiments, reflecting the importance of maintaining small residual corrections relative to the physics baseline.

Interpretation of the residual regularization. The L2 penalty on $NN_{residual}$ serves a fundamentally different purpose than the physics loss in soft-constraint approaches:

- **Soft-constraint physics loss:** Penalizes deviation of *predictions* from physics model \rightarrow network learns to match physics
- **Residual regularization:** Penalizes *magnitude* of corrections \rightarrow network learns minimal corrections necessary to explain data

This distinction is crucial: the residual regularization does not force the final prediction to match the physics model, but rather encourages parsimonious corrections. The network is free to learn large corrections where physics systematically fails, while defaulting to near-zero corrections where physics is accurate.

Key differences from soft-constraint approach. The physics-residual formulation differs fundamentally from soft constraints in three aspects:

1. **Guaranteed physics in every prediction.** Unlike soft constraints where physics compliance is encouraged through loss weighting, the additive formulation guarantees that every prediction contains the physics model contribution. Even if the residual network outputs zero, the prediction equals the physics model—a physically plausible baseline.
2. **Simplified learning objective.** The network learns the residual $y_{true} - \Phi_{H_2}^{phys}(\mathbf{x})$, which represents only the systematic deviation from physics predictions. This is a substantially simpler mapping than learning the full concentration field, as the physics model already captures the dominant trends with pressure, temperature, and current density.
3. **Regularization promotes extrapolation.** The L2 penalty on residual magnitude biases the network toward smaller corrections. At extrapolation conditions where the network has limited training signal, this regularization causes the residual to shrink toward zero, naturally defaulting to physics-based predictions. This is fundamentally different from soft constraints, where the network may produce arbitrary outputs far from training data.

Gradient flow analysis. During backpropagation, the total gradient with respect to network parameters θ is:

$$\frac{\partial \mathcal{L}_{total}}{\partial \theta} = \frac{2}{N} \sum_{k=1}^N \left[\left(\hat{y}_{final}^{(k)} - y_{true}^{(k)} \right) + \lambda \cdot \text{NN}_{residual}(\mathbf{x}^{(k)}) \right] \cdot \frac{\partial \text{NN}_{residual}(\mathbf{x}^{(k)})}{\partial \theta} \quad (22)$$

Both gradient terms flow through $\text{NN}_{residual}$ only, while $\Phi_{H_2}^{phys}$ has no learnable parameters. The physics model acts as a fixed computational anchor, contributing to predictions without participating in gradient-based optimization. The regularization term $\lambda \cdot \text{NN}_{residual}$ provides consistent gradient signal pushing residuals toward zero, independent of prediction error magnitude.

4.4 Training procedure

To ensure rigorous validation and reproducibility, we standardized the training hyperparameters across all architectures and implemented two distinct validation protocols tailored for interpolation and extrapolation assessment.

Hyperparameter Configuration: All models were optimized using **Adam** [49] with a fixed batch size of 32. The learning rate was initialized at $\eta = 1.5 \times 10^{-3}$. We employed an **Early Stopping** strategy with a patience of 150 epochs to prevent overfitting, setting the maximum training duration to **700 epochs**. For the Standard PINN baseline, the physics weight β followed an **adaptive linear decay schedule** (0.7 to 0.01) to balance physical guidance and data fidelity.

Validation Protocols:

1. **Interpolation & Stability:** To assess model accuracy and training stability within the experimental domain, we employed a **5-fold cross-validation** scheme. To account for stochastic initialization, each fold was repeated with **20 independent runs**, resulting in 100 trained instances per architecture. This extensive sampling allows for the robust estimation of performance variance reported in Figure 1.
2. **Extrapolation & Uncertainty Quantification:** For the extrapolation tests (Section 2.2) and uncertainty analysis (Section 2.5), we utilized a **Deep Ensemble** approach consisting of **100 independently trained models** [46]. These models were trained exclusively on data with cathode pressures ≤ 80 bar to strictly isolate the high-pressure extrapolation regime (120-200 bar). The ensemble training utilized the identical hyperparameter settings (700 epochs, early stopping) as the cross-validation runs to ensure consistency.

4.5 Uncertainty quantification

Prediction uncertainty was quantified using deep ensembles with 100 independently trained models. The ensemble configuration followed a systematic protocol: each model was initialized with sequential random seeds (base seed 42 + model index, where model index ranges from 0 to 99), trained for maximum 700 epochs with early stopping (patience 150 epochs, minimum delta 1e-6), using identical hyperparameters (learning rate 1.5e-3, batch size 32, Adam optimizer). This approach ensures reproducibility

while capturing both aleatoric uncertainty (inherent data noise) and epistemic uncertainty (model uncertainty). For extrapolation tests, the same 100-model ensemble was employed to generate robust confidence intervals shown in Figure 2.

The ensemble mean provided point predictions while the ensemble standard deviation quantified epistemic uncertainty. For sensitivity analysis, input perturbations followed typical operational variations or measurement uncertainties: ± 1 °C, ± 1 bar, ± 0.1 A/cm², ± 1 μ m.

Confidence intervals were constructed using the percentile method on ensemble predictions. Calibration was assessed by comparing the fraction of observations within predicted confidence intervals against nominal coverage probabilities.

4.6 Hardware benchmarking

Inference time measurements were conducted on three platforms: (1) Desktop PC: Intel Core i7-13700, 48 GB RAM, RTX-4060 GPU; (2) Edge GPU: NVIDIA Jetson AGX Orin, 64GB unified memory; (3) Edge CPU: Raspberry Pi 5, 8GB RAM. Each platform executed 1,000 forward passes with random inputs, discarding the first 100 for warm-up. Timing utilized high-resolution performance counters with microsecond precision.

4.7 Statistical analysis

Statistical analyses were performed using Python 3.10 with NumPy 1.24, SciPy 1.11, and scikit-learn 1.3. Model performance was evaluated using the coefficient of determination (R^2), root-mean-square error (RMSE), mean absolute error (MAE), and mean absolute percentage error (MAPE). For extrapolation tests beyond the training pressure range (1–80 bar), models were evaluated at 120, 160, and 200 bar with $n = 24$ total test samples (eight samples per pressure level, Nafion 117, 25°C).

Three-way performance comparisons among PR-Net, Standard PINN, and Pure NN employed a hierarchical testing strategy designed to control the family-wise error rate under non-normality. Normality of absolute error distributions for each architecture was assessed jointly via the Shapiro-Wilk test and D’Agostino K^2 test; distributions were classified as non-normal if either test yielded $p < 0.05$. As Standard PINN and Pure NN errors violated normality ($p < 0.001$ by both criteria), non-parametric procedures were adopted throughout.

Global differences across all three architectures were first assessed via the Friedman test [50], which is appropriate for matched, non-normally distributed data in small-sample settings. Upon rejection of the omnibus null hypothesis ($\alpha = 0.05$), pairwise post-hoc comparisons were conducted using one-sided Wilcoxon signed-rank tests [51] (alternative hypothesis: PR-Net MAE < comparator MAE) with Holm–Bonferroni correction applied across the three pairwise contrasts [52]. Corrected p -values below 0.05 were considered statistically significant. Effect sizes were quantified using rank-biserial correlation r , computed as:

$$r = \frac{W_+ - W_-}{n(n+1)/2} \quad (23)$$

where W_+ and W_- denote the sums of positive and negative signed ranks, respectively, and n is the number of non-zero differences. Effect magnitudes were interpreted as small ($|r| < 0.3$), medium ($0.3 \leq |r| < 0.5$), or large ($|r| \geq 0.5$) following established conventions for non-parametric effect sizes [53].

To assess whether performance divergence accelerated with extrapolation distance—a key claim of the physics-residual framework—MAE degradation slopes (%/bar) were estimated for each architecture via linear regression of pressure-stratified MAE against cathode pressure (120, 160, 200 bar). Slope ratios between architectures provided a quantitative proxy for the Model \times Pressure interaction effect. Non-parametric bootstrap confidence intervals (10,000 resamples, percentile method) for mean MAE differences were constructed to provide distribution-free validation of parametric effect estimates [54]. Post-hoc power analysis confirmed that the achieved statistical power exceeded 0.99 for detecting the observed effect sizes ($|r| \geq 0.87$) at $\alpha = 0.05$ for the given sample size. Pressure-specific performance metrics, full pairwise Wilcoxon results, and detailed statistical diagnostics are provided in Supplementary Information A.5.

4.8 Code and data availability

The complete codebase and processed datasets are available on GitHub at <https://github.com/Innovation4x/PR-Net>. Raw experimental data sources are cited in the Methods section, and detailed data distribution analyses are provided in the supplementary information with appropriate attribution to the original authors.

References

- [1] Carmo, M., Fritz, D.L., Mergel, J., Stolten, D.: A comprehensive review on pem water electrolysis. *International Journal of Hydrogen Energy* **38**, 4901–4934 (2013)
- [2] Grigoriev, S.A., Fateev, V.N., Bessarabov, D.G., Millet, P.: Current status, research trends, and challenges in water electrolysis science and technology. *International Journal of Hydrogen Energy* **45**, 26036–26058 (2020)
- [3] Shiva Kumar, S., Himabindu, V.: Hydrogen production by pem water electrolysis – a review. *Materials Science for Energy Technologies* **2**, 442–454 (2019)
- [4] Trinke, P., Bensmann, B., Hanke-Rauschenbach, R.: Current density effect on hydrogen permeation in pem water electrolyzers. *International Journal of Hydrogen Energy* **42**(21), 14355–14366 (2017) <https://doi.org/10.1016/j.ijhydene.2017.03.231>
- [5] Schalenbach, M., Carmo, M., Fritz, D.L., Mergel, J., Stolten, D.: Pressurized pem water electrolysis: Efficiency and gas crossover. *International Journal of Hydrogen Energy* **38**(35), 14921–14933 (2013) <https://doi.org/10.1016/j.ijhydene.2013.09.013>

- [6] Omrani, R., Shabani, B.: Hydrogen crossover in proton exchange membrane electrolyzers: The effect of current density, pressure, temperature, and compression. *Electrochimica Acta* **377**, 138085 (2021)
- [7] Feng, Q., Yuan, X.Z., Liu, G., Wei, B., Zhang, Z.: A review of proton exchange membrane water electrolysis on degradation mechanisms and mitigation strategies. *Journal of Power Sources* **366**, 33–55 (2017)
- [8] Schmidt, O., Gambhir, A., Staffell, I., Hawkes, A., Nelson, J.: Future cost and performance of water electrolysis: An expert elicitation study. *International Journal of Hydrogen Energy* **42**, 30470–30492 (2017)
- [9] Aubras, F., Deseure, J., Kadjo, J.J., Dedigama, I., Majasan, J.: Two-dimensional model of low-pressure pem electrolyser: Two-phase flow regime, electrochemical modelling and experimental validation. *International Journal of Hydrogen Energy* **42**, 26203–26216 (2017)
- [10] Han, B., Steen, S.M., Mo, J., Zhang, F.Y.: Electrochemical performance modeling of a proton exchange membrane electrolyzer cell for hydrogen production. *International Journal of Hydrogen Energy* **40**, 7006–7016 (2015)
- [11] Toghyani, S., Afshari, E., Baniasadi, E., Atyabi, S.A.: Thermal and electrochemical performance assessment of a high temperature pem electrolyzer. *Energy* **152**, 237–246 (2018)
- [12] Ni, M., Leung, M.K.H., Leung, D.Y.C.: Energy and exergy analysis of hydrogen production by a proton exchange membrane (pem) electrolyzer plant. *Energy Conversion and Management* **49**, 2748–2756 (2008)
- [13] García-Valverde, R., Espinosa, N., Urbina, A.: Simple pem water electrolyser model and experimental validation. *International Journal of Hydrogen Energy* **37**, 1927–1938 (2012)
- [14] Awasthi, A., Scott, K., Basu, S.: Dynamic modeling and simulation of a proton exchange membrane electrolyzer for hydrogen production. *International Journal of Hydrogen Energy* **36**, 14779–14786 (2011)
- [15] Mohamed, A., Ibrahim, H., Yang, R., Kim, K.: Optimization of proton exchange membrane electrolyzer cell design using machine learning. *Energies* **15**, 6657 (2022)
- [16] Ding, R., *et al.*: Machine learning utilized for the development of proton exchange membrane electrolyzers. *Journal of Power Sources* **556**, 232389 (2023) <https://doi.org/10.1016/j.jpowsour.2022.232389>
- [17] Chen, X., *et al.*: Machine learning in proton exchange membrane water electrolysis — a knowledge-integrated framework. *Applied Energy* **371**, 123550 (2024) <https://doi.org/10.1016/j.apenergy.2024.123550>

[//doi.org/10.1016/j.apenergy.2024.123550](https://doi.org/10.1016/j.apenergy.2024.123550)

- [18] Karniadakis, G.E., Kevrekidis, I.G., Lu, L., Perdikaris, P., Wang, S.: Physics-informed machine learning. *Nature Reviews Physics* **3**, 422–440 (2021)
- [19] Raissi, M., Perdikaris, P., Karniadakis, G.E.: Physics-informed neural networks: A deep learning framework for solving forward and inverse problems involving nonlinear partial differential equations. *Journal of Computational Physics* **378**, 686–707 (2019)
- [20] Karniadakis, G.E., *et al.*: Physics-informed machine learning. *Nature Reviews Physics* **3**, 422–440 (2021)
- [21] Sun, L., Gao, H., Pan, S., Wang, J.X.: Surrogate modeling for fluid flows based on physics-constrained deep learning without simulation data. *Computer Methods in Applied Mechanics and Engineering* **361**, 112732 (2020)
- [22] Jin, X., Cai, S., Li, H., Karniadakis, G.E.: Nsfnets (navier-stokes flow nets): Physics-informed neural networks for the incompressible navier-stokes equations. *Journal of Computational Physics* **426**, 109951 (2021)
- [23] Cai, S., Wang, Z., Wang, S., Perdikaris, P., Karniadakis, G.E.: Physics-informed neural networks for heat transfer problems. *Journal of Heat Transfer* **143**, 060801 (2021)
- [24] Zerrougui, I., Li, Z., Hissel, D.: Physics-informed neural network for modeling and predicting temperature fluctuations in proton exchange membrane electrolysis. *Energy AI* **20**, 100474 (2025) <https://doi.org/10.1016/j.egyai.2025.100474>
- [25] Ko, T., Kim, D., Park, J., Lee, S.H.: Physics-informed neural network for long-term prognostics of proton exchange membrane fuel cells. *Applied Energy* **382**, 125318 (2025) <https://doi.org/10.1016/j.apenergy.2025.125318>
- [26] Polo-Molina, A., *et al.*: Modeling membrane degradation in pem electrolyzers with physics-informed neural networks. arXiv preprint arXiv:2507.02887 (2025)
- [27] Chen, Z., Xiu, D.: On generalized residual network for deep learning of unknown dynamical systems. *Journal of Computational Physics* **438**, 110362 (2021) <https://doi.org/10.1016/j.jcp.2021.110362>
- [28] Jia, X., Willard, J., Karpatne, A., Read, J.S., Zwart, J.A., Steinbach, M., Kumar, V.: Physics-guided machine learning for scientific discovery: An application in simulating lake temperature profiles. *ACM/IMS Transactions on Data Science* **2**(3), 1–26 (2021) <https://doi.org/10.1145/3447814>
- [29] Wu, J., Zhang, G., Dong, B., Chang, Y., Chen, Y.: Experimental and simulation

- study of h₂ crossover in pem water electrolysis for high-pressure hydrogen production up to 20 mpa. *International Journal of Hydrogen Energy* **135**, 499–506 (2025) <https://doi.org/10.1016/j.ijhydene.2025.04.404>
- [30] Yao, Y., *et al.*: Hydrogen energy industry in china: The current status, safety problems, and pathways for future safe and healthy development. *Safety Science* **186**, 106808 (2025) <https://doi.org/10.1016/j.ssci.2025.106808>
- [31] Sakai, T., Takenaka, H., Torikai, E.: Gas diffusion in the dried and hydrated nafions. *Journal of The Electrochemical Society* **133**, 88–92 (1986)
- [32] International Organization for Standardization: ISO 26142:2010 — Hydrogen detection apparatus — Stationary applications. Includes performance requirements such as response time; specifies $t_{90} \leq 30$ s for the response time definition used in the standard (2010)
- [33] Hübner, T., Banach, U.: Time response of hydrogen sensors. In: International Conference on Hydrogen Safety (ICHS) (2013). Reports response times measured according to ISO 26142, with typical t_{90} values on the order of seconds
- [34] Buttner, W.J., Post, M.B., Burgess, R., Rivkin, C.: An overview of hydrogen safety sensors and requirements. *International Journal of Hydrogen Energy* **36**, 2462–2470 (2011)
- [35] International Energy Agency: The Future of Hydrogen: Seizing Today’s Opportunities. IEA Publications, ??? (2019)
- [36] Peng, D.-Y., Robinson, D.B.: A new two-constant equation of state. *Industrial & Engineering Chemistry Fundamentals* **15**(1), 59–64 (1976) <https://doi.org/10.1021/i160057a011>
- [37] International Energy Agency: The future of hydrogen: Seizing today’s opportunities. Technical report, IEA Publications (2019). <https://www.iea.org/reports/the-future-of-hydrogen>
- [38] Tao, L., *et al.*: Present and future cost of alkaline and PEM electrolyser stacks. *International Journal of Hydrogen Energy* **48**(83), 32313–32330 (2023) <https://doi.org/10.1016/j.ijhydene.2023.05.031>
- [39] Mayyas, A., Ruth, M., Pivovar, B., Bender, G., Wipke, K.: Manufacturing cost analysis for proton exchange membrane water electrolyzers. Technical Report NREL/TP-6A20-72740, National Renewable Energy Laboratory (2019). <https://www.nrel.gov/docs/fy19osti/72740.pdf>
- [40] Faroughi, S.A., *et al.*: Physics-guided, physics-informed, and physics-encoded neural networks and operators in scientific computing: Fluid and solid mechanics. *Journal of Computing and Information Science in Engineering* **24**, 040802 (2024)

- [41] Grigoriev, S.A., Porembskiy, V.I., Korobtsev, S.V., Fateev, V.N., Auprêtre, F., Millét, P.: High-pressure pem water electrolysis and corresponding safety issues. *International Journal of Hydrogen Energy* **36**(3), 2721–2728 (2011) <https://doi.org/10.1016/j.ijhydene.2010.03.058>
- [42] Garbe, S., Babic, U., Nilsson, E., Schmidt, T.J., Gubler, L.: Communication—pt-doped thin membranes for gas crossover suppression in polymer electrolyte water electrolysis. *Journal of The Electrochemical Society* **166**(13), 873 (2019) <https://doi.org/10.1149/2.0111913jes>
- [43] Stähler, M., Stähler, A., Scheepers, F., Carmo, M., Lehnert, W., Stolten, D.: Impact of porous transport layer compression on hydrogen permeation in pem water electrolysis. *International Journal of Hydrogen Energy* **45**(7), 4008–4014 (2020) <https://doi.org/10.1016/j.ijhydene.2019.12.016>
- [44] Martin, A., Abbas, D., Trinke, P., Böhm, T., Bierling, M., Bensmann, B., Thiele, S., Hanke-Rauschenbach, R.: Communication—proving the importance of pt-interlayer position in pemwe membranes for the effective reduction of the anodic hydrogen content. *Journal of The Electrochemical Society* **168**(9), 094509 (2021) <https://doi.org/10.1149/1945-7111/ac275b>
- [45] Bernt, M., Schröter, J., Möckl, M., Gasteiger, H.A.: Analysis of gas permeation phenomena in a pem water electrolyzer operated at high pressure and high current density. *Journal of The Electrochemical Society* **167**(12), 124502 (2020) <https://doi.org/10.1149/1945-7111/abaa68>
- [46] Lakshminarayanan, B., Pritzel, A., Blundell, C.: Simple and scalable predictive uncertainty estimation using deep ensembles. In: *Advances in Neural Information Processing Systems*, vol. 30 (2017)
- [47] Es'kin, V.A., Malkhanov, A.O., Smorkalov, M.E.: Are two hidden layers still enough for the physics-informed neural networks? arXiv preprint arXiv:2412.19235 (2024)
- [48] Glorot, X., Bengio, Y.: Understanding the difficulty of training deep feedforward neural networks. In: *Proceedings of the 13th International Conference on Artificial Intelligence and Statistics*, pp. 249–256 (2010)
- [49] Kingma, D.P., Ba, J.: Adam: A method for stochastic optimization. arXiv preprint arXiv:1412.6980 (2014)
- [50] Friedman, M.: The use of ranks to avoid the assumption of normality implicit in the analysis of variance. *Journal of the American Statistical Association* **32**(200), 675–701 (1937) <https://doi.org/10.1080/01621459.1937.10503522>
- [51] Wilcoxon, F.: Individual comparisons by ranking methods. *Biometrics Bulletin* **1**(6), 80–83 (1945) <https://doi.org/10.2307/3001968>

- [52] Holm, S.: A simple sequentially rejective multiple test procedure. *Scandinavian Journal of Statistics* **6**(2), 65–70 (1979)
- [53] Kerby, D.S.: The simple difference formula: An approach to teaching nonparametric correlation. *Comprehensive Psychology* **3**, 11–31 (2014) <https://doi.org/10.2466/11.IT.3.1>
- [54] Efron, B., Tibshirani, R.: *An introduction to the bootstrap*. CRC Press (1994)
- [55] Zhu, J., Lai, X., Zhu, Z., Ke, P., Zheng, Y., Tang, X., Li, X., Yuan, Y., Chong, H., Yan, C., Wang, Y., Lin, Y., Zhou, X., Chen, Y.: Online generation of full-frequency electrochemical impedance spectra for lithium-ion batteries using early-stage partial relaxation voltage curve. *eTransportation* **26**, 100482 (2025) <https://doi.org/10.1016/j.etrans.2025.100482>
- [56] Wang, F., Zhai, Z., Zhao, Z., Di, Y., Chen, X.: Physics-informed neural network for lithium-ion battery degradation stable modeling and prognosis. *Nature Communications* **15**(1), 4332 (2024) <https://doi.org/10.1038/s41467-024-48779-z>

A Supplementary Information

A.1 Supplementary Figures

A.1.1 Dataset Analysis Figures

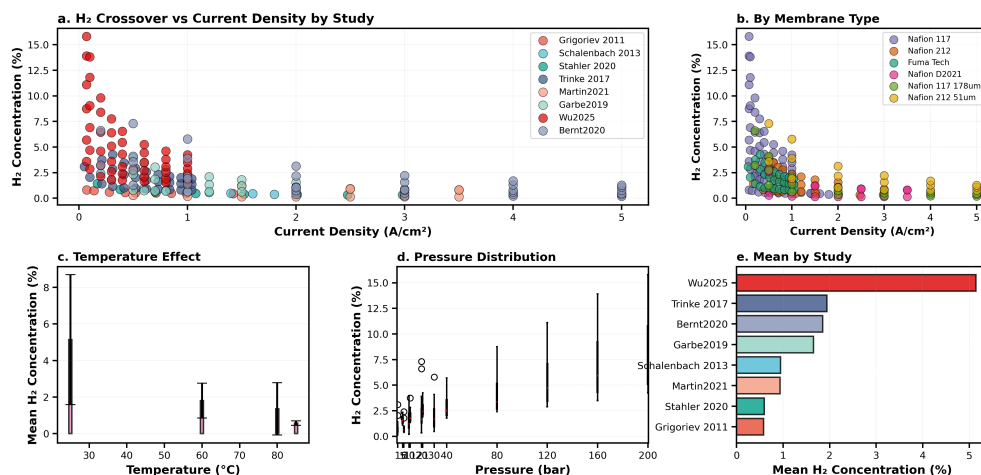


Fig. S1 Compiled experimental dataset characterisation: operating condition coverage and study-specific crossover distributions ($n = 184$). **a**, Relationship between H₂ crossover concentration and current density across eight independent studies ($n = 184$ data points). **b**, Membrane-specific H₂ crossover behaviour for six membrane types under varying current densities (0.05–5.00 A cm⁻²). **c**, Temperature dependence of mean H₂ concentration across the operating range of 25–85°C. Error bars represent ± 1 s.d. **d**, Distribution of H₂ concentration as a function of operating pressure (1–200 bar). Box plots show median, interquartile range, and outliers. **e**, Study-specific mean H₂ crossover concentrations, illustrating the wide inter-study variability in measured crossover rates across the compiled dataset. Data compiled from Grigoriev et al. (2011), Schalenbach et al. (2013), Stähler et al. (2020), Trinke et al. (2017), Martin et al. (2021), Garbe et al. (2019), Wu et al. (2025), and Bernt et al. (2020).

Statistical Analysis of H₂ Crossover

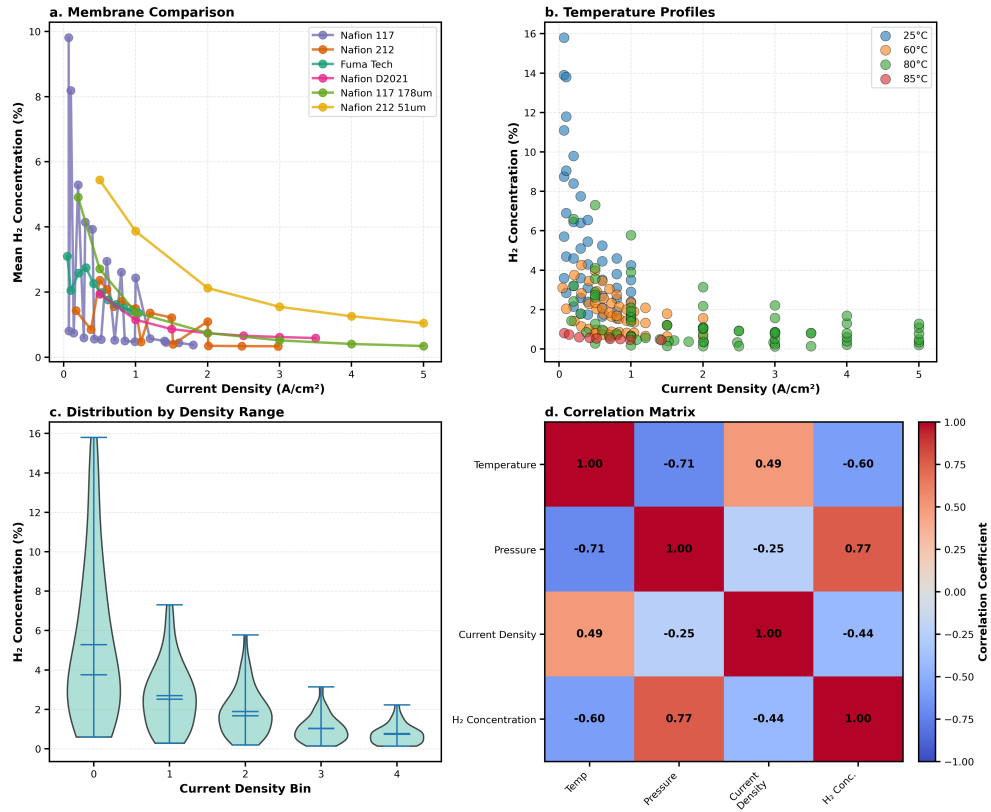


Fig. S2 Membrane-type crossover trends, temperature-dependent concentration profiles, and inter-parameter correlation structure for the compiled experimental dataset. **a**, Comparative analysis of mean H₂ crossover trends for six membrane types (Nafion 117, Nafion 212, FumaTech E-730, Nafion D2021, Nafion 117 178 μm , Nafion 212 51 μm) as a function of current density (0–5 A cm⁻²). **b**, Temperature-dependent H₂ concentration profiles at four operating temperatures (25, 60, 80, and 85°C) across the full current density range. **c**, Violin plots illustrating the concentration distribution and probability density of H₂ concentration within discrete current density intervals, revealing the concentration spread and median values across operating conditions. **d**, Pearson correlation matrix depicting pairwise relationships between key operational parameters (temperature, pressure, current density) and H₂ crossover concentration. Pressure demonstrates the strongest positive correlation with H₂ concentration ($r = 0.77$), while temperature and current density exhibit moderate negative associations ($r = -0.71$ and $r = -0.44$, respectively).

Operating Conditions Impact Analysis

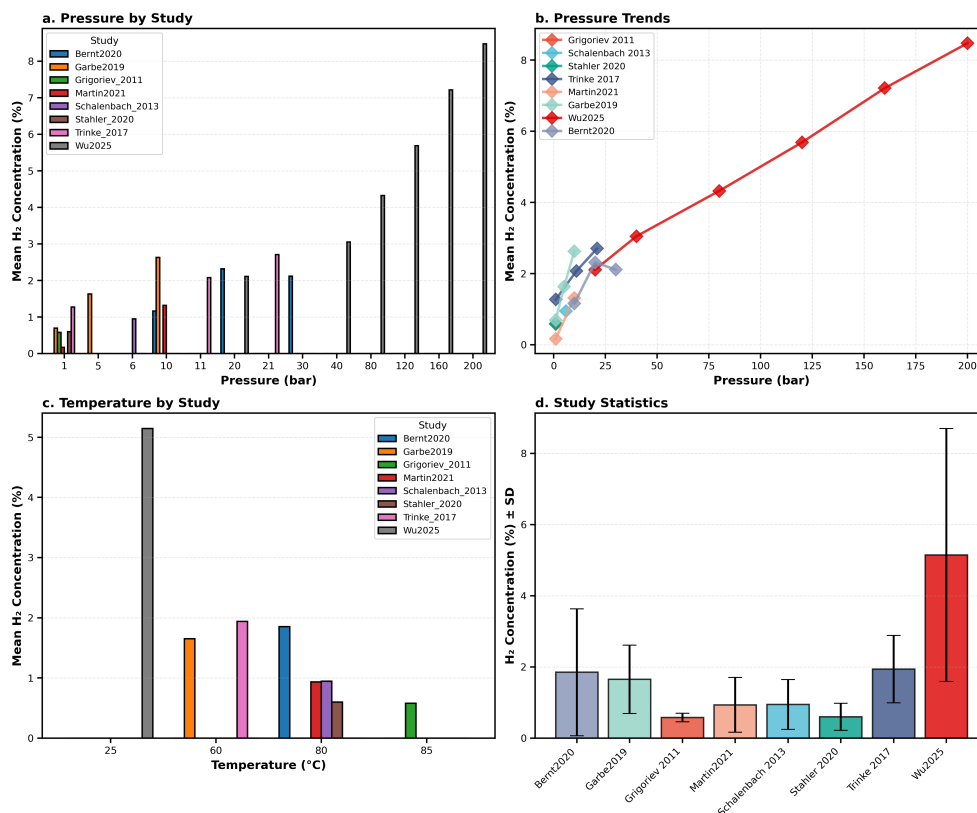


Fig. S3 Study-stratified pressure sensitivity and thermal response of hydrogen crossover across the compiled experimental dataset. **a**, Study-specific mean H₂ concentration at discrete cathode pressure conditions (1–200 bar), revealing pressure-dependent crossover behaviour across eight independent studies. **b**, Pressure-dependent H₂ concentration trends for individual studies, illustrating marked inter-study variability in pressure sensitivity across the full operating range (1–200 bar). **c**, Temperature-dependent H₂ concentration profiles at four operating temperatures (25, 60, 80, and 85°C), showing study-specific thermal responses across the compiled dataset. **d**, Study-stratified mean H₂ crossover concentrations with ± 1 s.d. error bars. Per-study sample sizes and descriptive statistics (mean \pm s.d.): Bernt et al. 2020 ($n = 37$, $1.85 \pm 1.78\%$), Garbe et al. 2019 ($n = 24$, $1.65 \pm 0.96\%$), Grigoriev et al. 2011 ($n = 9$, $0.58 \pm 0.12\%$), Martin et al. 2021 ($n = 21$, $0.94 \pm 0.77\%$), Schalenbach et al. 2013 ($n = 9$, $0.95 \pm 0.70\%$), Stähler et al. 2020 ($n = 8$, $0.60 \pm 0.38\%$), Trinke et al. 2017 ($n = 28$, $1.94 \pm 0.95\%$), Wu et al. 2025 ($n = 48$, $5.14 \pm 3.55\%$); total $n = 184$.

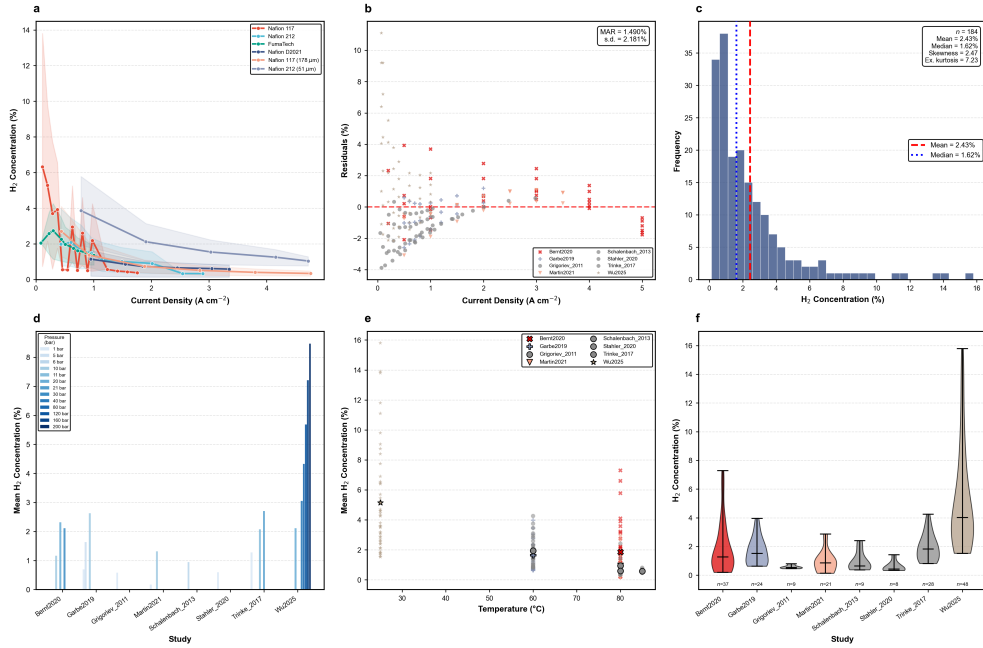


Fig. S4 Membrane-specific crossover performance envelopes, dataset-wide concentration distribution, and inter-study variability characterisation ($n = 184$). **a**, Membrane-specific H_2 crossover performance across the current density range ($0\text{--}5\text{ A cm}^{-2}$) with min–max shaded regions indicating the full observed concentration envelope: Nafion 117 ($n = 66$; $0.38\text{--}15.80\%$), Nafion 212 ($n = 32$; $0.34\text{--}3.97\%$), FumaTech E-730 ($n = 28$; $0.82\text{--}4.26\%$), Nafion D2021 ($n = 21$; $0.14\text{--}2.88\%$), Nafion 117 $178\text{ }\mu\text{m}$ ($n = 20$; $0.20\text{--}6.60\%$), Nafion 212 $51\text{ }\mu\text{m}$ ($n = 17$; $0.77\text{--}7.30\%$). **b**, Residuals from a quadratic polynomial fit of H_2 concentration versus current density across all studies (mean absolute residual: 1.490% ; s.d.: 2.181%), characterising the non-linear variability and inter-study scatter in the compiled experimental dataset beyond a second-order trend. **c**, Histogram of the overall H_2 concentration distribution across the compiled dataset ($n = 184$; mean = 2.43% , median = 1.62% ; skewness = 2.47 , excess kurtosis = 7.23), indicating a right-skewed, leptokurtic distribution consistent with the predominance of low-crossover operating conditions in the compiled studies. **d**, Study-stratified mean H_2 concentration at each discrete cathode pressure level ($1\text{--}200\text{ bar}$), presented as grouped bars per study with pressure indicated by colour intensity (light to dark blue: 1 to 200 bar). The pronounced increase in mean crossover concentration at high pressures ($\geq 120\text{ bar}$) is confined to studies employing elevated-pressure test protocols, illustrating the heterogeneous pressure coverage among the eight contributing studies. **e**, Individual H_2 concentration measurements as a function of operating temperature ($25\text{--}85^\circ\text{C}$) for each contributing study, with study-specific markers and colours. The sparse temperature coverage of most studies reflects the predominance of isothermal experimental designs in the compiled dataset. **f**, Violin plots illustrating the H_2 concentration distribution and probability density for each contributing study, with per-study sample sizes annotated below each violin (Bernt2020: $n = 37$; Garbe2019: $n = 24$; Grigoriev2011: $n = 9$; Martin2021: $n = 21$; Schalenbach2013: $n = 9$; Stähler2020: $n = 8$; Trinke2017: $n = 28$; Wu2025: $n = 48$). The markedly broader distribution of Wu2025 reflects its extended high-pressure experimental range ($1\text{--}200\text{ bar}$), in contrast to the narrower distributions of studies conducted at lower operating pressures.

A.1.2 Membrane Comparison Figures

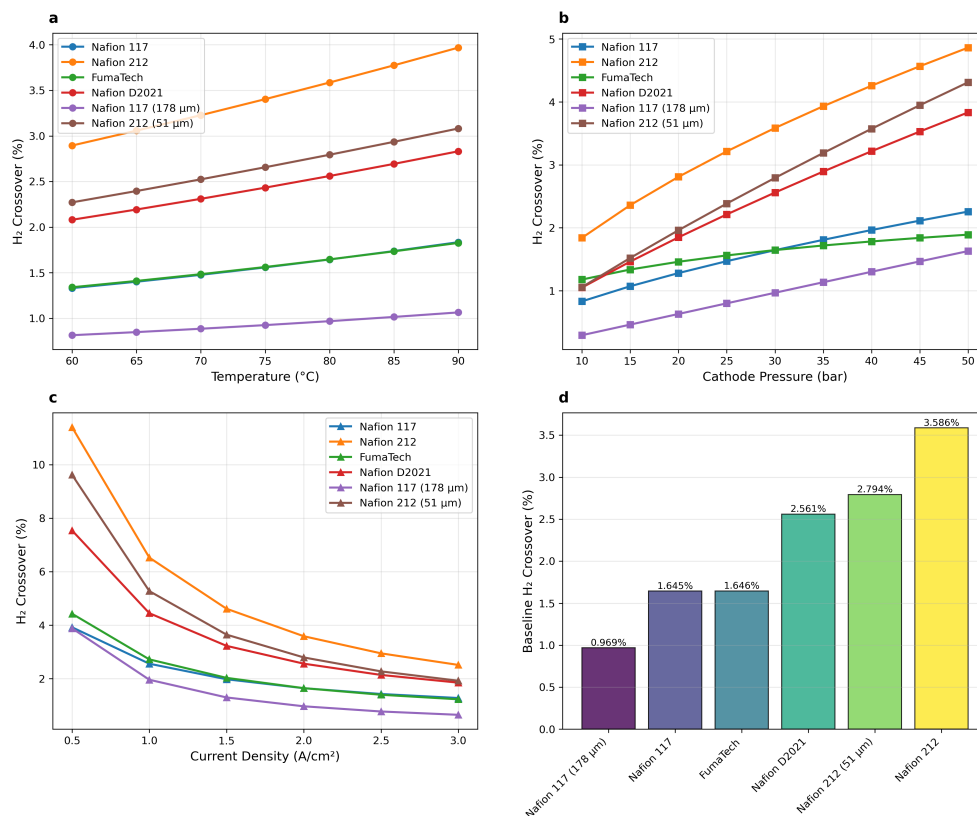


Fig. S5 Membrane-type-dependent hydrogen crossover responses to temperature, pressure, and current density under controlled operating conditions ($n = 184$ experimental points across six membrane types). **a**, Temperature dependence of H_2 crossover at 2.0 A cm^{-2} and 10 bar, showing minimal variation ($<5\%$ change) for thick membranes but a pronounced increase for thinner membranes (Nafion 212 ($51 \mu\text{m}$): 14.8% increase from 60 to 85°C). **b**, Pressure response at 80°C and 1.0 A cm^{-2} , demonstrating thickness-dependent crossover scaling (Nafion 212 ($51 \mu\text{m}$): 2.75-fold increase over 10–50 bar), with sub-linear pressure dependence above 30 bar consistent with increasing membrane transport resistance at elevated pressures. **c**, Current density dependence at 80°C and 30 bar. On a linear scale, a macroscopic transition from diffusion-dominated crossover ($i < 1.0 \text{ A cm}^{-2}$) towards a Faradaic-recombination-limited regime ($i > 2.0 \text{ A cm}^{-2}$) is apparent; the precise mechanistic inflection point identified via logarithmic analysis is discussed in the main text. **d**, Membrane performance ranking at reference conditions (80°C , 10 bar, 2.0 A cm^{-2}), with Nafion 117 ($178 \mu\text{m}$) exhibiting the lowest baseline crossover concentration (0.969% H_2) among the evaluated materials.

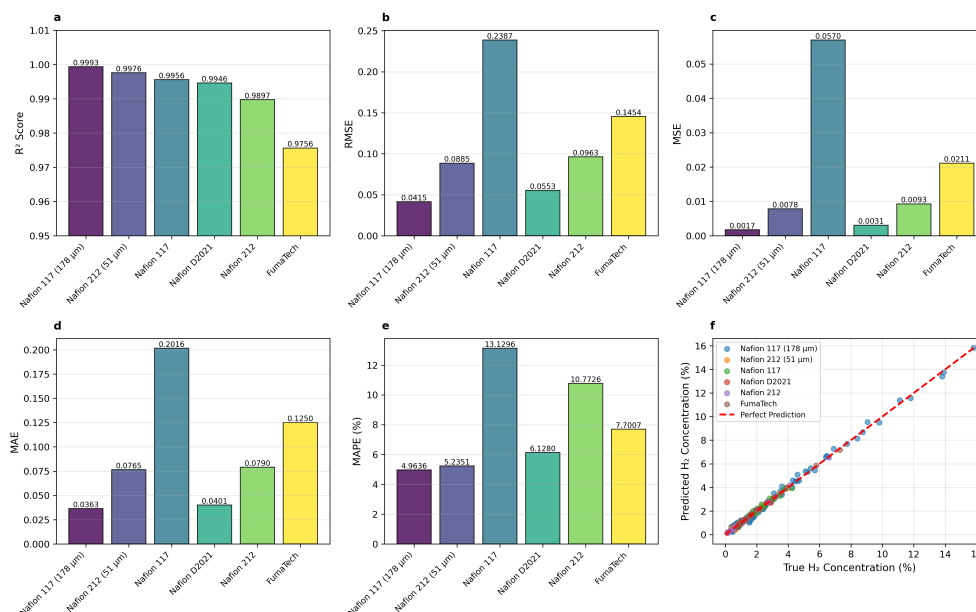


Fig. S6 PR-Net predictive accuracy across all six membrane types evaluated on the full experimental dataset via repeated cross-validation ($n = 184$). **a–e**, Membrane-stratified performance metrics (R^2 , RMSE, MSE, MAE, and MAPE) derived from out-of-fold predictions of a repeated cross-validation procedure (20 repeats \times 5 folds; $n_{\text{models}} = 100$) without data augmentation. $R^2 \geq 0.975$ for all membrane types, with Nafion 117 (178 μm) and Nafion 212 (51 μm) achieving the highest coefficients of determination ($R^2 = 0.9993$ and 0.9976 , respectively). Nafion 117 exhibits the largest absolute errors (RMSE = 0.239%; MAE = 0.202%), attributable to its broad experimental concentration range (0.38–15.80%) which spans the widest dynamic range among the six membrane types. Correspondingly, MAPE is highest for Nafion 117 (13.13%) and Nafion 212 (10.77%), reflecting the relative difficulty of percentage-based error metrics at low absolute concentration values present in these datasets. In contrast, thinner membranes (Nafion 117 178 μm , Nafion 212 51 μm , and Nafion D2021) achieve RMSE $\leq 0.089\%$ and MAPE $\leq 6.13\%$, consistent with their narrower and more uniform concentration ranges. Cross-validation metrics represent conservative performance estimates under held-out test conditions. **f**, Parity plot of PR-Net out-of-fold predictions versus experimental measurements across all six membrane types (overall $R^2 = 0.9960$). The red dashed line indicates perfect agreement. Membrane-specific clustering along the parity line confirms that the PR-Net hard-constraint architecture captures material transport characteristics consistently across structurally and chemically diverse ionomer membranes spanning a 40-fold range in crossover concentration.

A.2 Supplementary Tables

Table S1 Membrane-Specific Operating Conditions. Summary of experimental conditions for each membrane type in the training dataset ($n = 184$ experimental points).

Membrane Type	Temperature (°C)	Pressure Range (bar)	Current Density (A/cm ²)	Thickness (µm)	Data Points
Nafion 117	25, 80, 85	1–200	0.07–1.80	209	66
Nafion 212	60, 80	1–10	0.17–2.98	58	32
Nafion D2021	80	1–10	0.50–3.50	110	21
FumaTech E-730	60	1–21	0.05–1.04	260	28
Nafion 117 (178 µm)	80	10–30	0.20–5.00	178	20
Nafion 212 (51 µm)	80	10–30	0.50–5.00	51	17

Table S2 Extrapolation performance comparison of three modelling architectures at unseen high-pressure test conditions (120, 160, and 200 bar). Models were trained exclusively on Nafion 117 data with cathode pressures ≤ 80 bar ($n = 42$) and evaluated on a fully held-out test set ($n = 24$; Wu et al. [29], 25°C). Values represent mean \pm standard deviation across 100 independently trained ensemble members. RMSE and MAE metrics quantify the absolute prediction error in actual H₂ percentage.

Method (Integration)	R^2 (%)				Overall RMSE	Overall MAE
	120 bar	160 bar	200 bar	Overall	(% H ₂)	(% H ₂)
PR-Net (Hard-constraint)	99.61 \pm 0.14	98.80 \pm 0.35	97.34 \pm 0.69	98.49 \pm 0.36	0.45 \pm 0.05	0.38 \pm 0.04
Standard PINN (Soft-constraint)	95.02 \pm 0.69	84.00 \pm 1.98	71.72 \pm 2.88	82.71 \pm 1.89	1.54 \pm 0.08	0.99 \pm 0.06
Pure NN (Data-driven)	90.75 \pm 2.31	73.46 \pm 5.38	58.00 \pm 8.60	73.10 \pm 5.53	1.91 \pm 0.20	1.52 \pm 0.15

Table S3 Interpolation performance comparison on the training domain. Performance metrics derived from repeated 5-fold cross-validation (100 independent models per architecture) evaluated on the 184 experimental data points. Values represent mean \pm standard deviation. The PR-Net hard-constraint architecture significantly reduces error variance and improves overall accuracy compared to baseline approaches.

Method	Architecture	R^2 (%)	RMSE (%)	MAE (%)	MAPE (%)
PR-Net (ours)	Hard-constraint	99.57 \pm 0.16	0.167 \pm 0.025	0.124 \pm 0.019	9.73 \pm 1.73
Standard PINN	Soft-constraint	99.00 \pm 1.14	0.236 \pm 0.102	0.156 \pm 0.061	12.40 \pm 4.76
Pure NN	None (data-driven)	96.47 \pm 6.20	0.325 \pm 0.216	0.218 \pm 0.157	18.93 \pm 15.94
Physics-only	Analytical baseline	99.47	0.193	0.140	10.93

[†] Physics-only model is a single deterministic analytical model with no stochastic components; standard deviation is not applicable.

Table S4 Computational Requirements. Hardware specifications and computational performance metrics.

Platform	CPU/GPU	RAM	Model Loading (ms)	Single Inference (ms)	Batch-100 (ms)	Power (W)
Desktop	i7-13700	48GB	125	0.31 \pm 0.04	28.7	125
Jetson AGX Orin	ARM A78AE + GPU	64GB	340	1.36 \pm 0.03	122.1	40
Raspberry Pi 5	ARM Cortex-A76	8GB	1850	1.08 \pm 0.34	99.8	16

Table S5 Detailed Cross-Validation and Ensemble Configuration

Parameter	5-Fold CV Configuration	Deep Ensemble Configuration
Number of folds/models	5 folds	100 models
Repetitions	20 independent runs	N/A (single run per model)
Total training runs	100 (5×20)	100
Random seed strategy	42 + (rep_idx \times 5)	42 + model_idx
Stratification	By membrane type	N/A
Training data	All 184 points (stratified 80/20 per fold)	≤ 80 bar only ($n = 42$)
Test data	20% held-out per fold (OOF)	120, 160, 200 bar ($n = 24$)
Training epochs (max)	700	700
Early stopping patience	150 epochs	150 epochs
Early stopping delta	1e-6	1e-6
Learning rate	1.5e-3	1.5e-3
Optimizer	Adam	Adam
Batch size	32	32
Physics weight β (Standard PINN)	Linear decay: 0.7 \rightarrow 0.01 over training	Linear decay: 0.7 \rightarrow 0.01 over training
Residual weight λ (PR-Net)	2.0 (fixed)	2.0 (fixed)
Purpose	Interpolation accuracy & training stability comparison	Uncertainty quantification & extrapolation robustness

A.3 Supplementary Analysis: Comparative Analysis with Recent PINN Applications

A.4 Supplementary Analysis: Comparative Analysis with Recent PINN Applications

Table S6 State-of-the-Art PINN Applications in Electrochemical Systems (2024–2025)

Application	System	Key Innovation	Performance	Data Efficiency	Reference
H₂ Crossover (This work)	PEM Electrolyzer	First systematic comparison of Pure NN, Standard PINN, and hard-constraint PR-Net for gas crossover; multi-membrane validation across six membrane types	$R^2 = 99.57\% \pm 0.16\%$ (CV); $R^2 = 0.9960$, RMSE = 0.167% (OOF ensemble)	184 experimental points; no synthetic data augmentation	This work
Temperature Prediction	PEM Electrolyzer	0D/1D models; parameter identification	MSE = 0.1596 (vs LSTM 1.2132)	Robust to sensor noise	Energy AI 2025 [24]
RUL Prediction	PEM Fuel Cell	Membrane/catalyst degradation physics	9.2% improvement over SOTA	26% input data requirement	Applied Energy 2025 [25]
Membrane Degradation	PEM Electrolyzer	Coupled ODEs for thinning & voltage	Captures long-term dynamics	Limited noisy data handling	arXiv 2025 [26]
EIS Generation	Li-ion Battery	Relaxation voltage → full EIS	<6.1% error	Insensitive to SOC/SOH	eTransportation 2025 [55]
Battery SOH	Li-ion (NCM)	Physics-informed NN degradation prognosis	Stable SOH prediction	Long-term cycling data	Nature Comm. 2024 [56]

A.4.1 Methodological Advances in PINN Architecture

Recent developments in PINN architectures have informed our design choices:

- Multi-Physics Coupling:** The PINN framework for electrokinetic microfluidic systems demonstrated exceptional accuracy (0.02% error) for coupled Nernst-Planck-Poisson-Navier-Stokes equations, validating our approach of incorporating multiple physical constraints (Fick’s law, Henry’s law, Faraday’s law) simultaneously.
- Domain Decomposition:** XPINNs (eXtended PINNs) enable space-time domain decomposition for complex geometries, suggesting future extensions for modeling spatially-resolved crossover in large-scale stacks.
- Adaptive Sampling:** Adversarial Adaptive Sampling (AAS) using optimal transport theory ensures smooth residual profiles, which could enhance our model’s performance in high-gradient regions near membrane interfaces.

A.4.2 Integration with Impedance Spectroscopy

The synergy between PINNs and electrochemical impedance spectroscopy (EIS) presents promising avenues:

- The Loewner framework enables data-driven extraction of distribution of relaxation times (DRT) from EIS data, which could identify rate-limiting processes affecting crossover
- Dynamic EIS (DEIS) allows real-time monitoring during charging/discharging, complementing our steady-state crossover predictions
- EIS analysis of PEM electrolyzers reveals distinct resistance contributions from kinetic, ohmic, and mass transport processes, each influencing crossover differently

A.4.3 Computational Efficiency Comparison

The PR-Net achieves millisecond-level inference on desktop and edge GPU platforms, with 1.08 ± 0.34 ms on a resource-constrained Raspberry Pi 5—well within the $t_{90} \leq 30$ s response-time requirement specified by ISO 26142 for stationary hydrogen detection. This compares favorably with recent implementations:

- Microfluidic PINN: 100–200 min training, high accuracy with sparse points
- Thermal PINN for bridges: Transfer learning reduces computation vs FEM
- Multi-scale CFD for PEMWE: Requires extensive computational resources

A.5 Supplementary Analysis: Statistical Analysis of Extrapolation Performance

A.5.1 Extrapolation Test Design and Statistical Validation

To rigorously assess the extrapolation capabilities of the three architectures—PR-Net, Standard PINN, and Pure NN—we conducted comprehensive statistical analyses on pressure conditions substantially beyond the training domain.

Training conditions:

- Pressure: 1.0–80.0 bar
- Current density: 0.07–1.8 A cm⁻²
- Membrane: Nafion 117
- Temperature: 25–85°C
- Total training samples: 42

Test conditions:

- Pressure: 120.0–200.0 bar (1.5–2.5× beyond training range)
- Current density: 0.07–1.00 A cm⁻²
- Membrane: Nafion 117
- Temperature: 25°C
- Total test samples: 24 (eight samples per pressure level)

A.5.2 Statistical Analysis Framework

Three-way performance comparisons employed a hierarchical non-parametric testing strategy. Table S7 summarises the statistical tests applied at each level of the analysis.

Table S7 Statistical testing framework for three-way model comparison.

Analysis level	Method
Omnibus test	Friedman test (matched, non-parametric)
Post-hoc	Wilcoxon signed-rank + Holm–Bonferroni correction (3 pairs)
Effect size	Rank-biserial correlation r
Confidence intervals	Bootstrap (percentile method, 10,000 resamples)
Interaction	MAE degradation slope per model (%/bar)

A.5.3 Normality Assessment

Normality of absolute error distributions was assessed jointly via the Shapiro-Wilk (SW) test and D’Agostino’s K^2 test. Distributions were classified as non-normal if either test yielded $p < 0.05$. Results are summarised in Table S8.

As Standard PINN and Pure NN errors departed significantly from normality ($p < 0.001$ by both criteria), non-parametric procedures were adopted throughout. The PR-Net error distribution was consistent with normality ($p = 0.094$), reflecting the stabilising effect of the hard-constraint physics backbone on prediction behaviour.

Table S8 Normality assessment of absolute prediction error distributions for each architecture ($n = 24$).

Model	SW stat	SW p	K^2 stat	K^2 p	Normal?
PR-Net	0.929	0.094	1.750	0.417	Yes
Standard PINN	0.779	<0.001	18.321	<0.001	No
Pure NN	0.844	0.002	13.285	0.001	No

A.5.4 Omnibus and Post-hoc Results

The Friedman omnibus test confirmed globally significant performance differences among the three architectures ($\chi^2 = 35.58$, $p < 0.001$). Pairwise post-hoc Wilcoxon signed-rank tests (one-sided; alternative hypothesis: Model A MAE < Model B MAE) with Holm–Bonferroni correction were subsequently applied. Results are presented in Table S9.

Table S9 Post-hoc pairwise Wilcoxon signed-rank test results with Holm–Bonferroni correction ($n = 24$). Effect sizes are quantified using rank-biserial correlation r ; $|r| \geq 0.5$ denotes a large effect.

Pair	W	raw p	adj p	Reject	r (RBC)	Effect
PR-Net < Standard PINN	19.0	0.000018	0.000018	Yes	−0.873	Large
PR-Net < Pure NN	1.0	<0.0001	<0.0001	Yes	−0.993	Large
Standard PINN < Pure NN	1.0	<0.0001	<0.0001	Yes	−0.993	Large

All three pairwise comparisons were statistically significant after multiple comparison correction, with all effect sizes classified as large ($|r| \geq 0.87$).

A.5.5 Bootstrap Confidence Intervals

Non-parametric bootstrap confidence intervals (percentile method, 10,000 resamples) for mean MAE differences (Model A – Model B) are presented in Table S10. All intervals exclude zero, confirming the practical as well as statistical significance of the observed differences.

Table S10 Bootstrap confidence intervals (95%, percentile method, 10,000 resamples) for mean absolute error differences. A negative difference indicates that Model A achieves lower MAE than Model B.

Pair (A vs B)	Mean diff (%)	95% CI lower	95% CI upper
PR-Net vs Standard PINN	−0.726	−1.165	−0.376
PR-Net vs Pure NN	−1.149	−1.588	−0.778
Standard PINN vs Pure NN	−0.422	−0.556	−0.296

A.5.6 Pressure-Stratified Performance

Table S11 presents mean absolute errors stratified by cathode pressure. The progressive widening of the performance gap with increasing extrapolation distance is evident across all three pressure levels.

Table S11 Pressure-stratified mean absolute error (MAE, mean \pm s.d.) for the three architectures at extrapolation pressures.

Pressure	PR-Net (MAE, %)	Standard PINN (MAE, %)	Pure NN (MAE, %)
120 bar	0.145 \pm 0.089	0.403 \pm 0.406	0.691 \pm 0.477
160 bar	0.348 \pm 0.175	1.144 \pm 0.905	1.579 \pm 0.948
200 bar	0.631 \pm 0.171	1.756 \pm 1.274	2.300 \pm 1.220

A.5.7 Model \times Pressure Interaction Analysis

To quantify the rate at which performance diverges with extrapolation distance, MAE degradation slopes (%/bar) were estimated for each architecture via linear regression of pressure-stratified mean absolute errors against cathode pressure. As slopes were estimated from three data points (degrees of freedom = 1), these values serve as descriptive indices of degradation rate and are interpreted in conjunction with the pressure-stratified Wilcoxon results in Section A.5.8.

Table S12 MAE degradation slopes and relative acceleration ratios for the three architectures.

Model	Slope (%/bar)	Ratio vs PR-Net	Ratio vs Std PINN
PR-Net	0.0061	1.00 \times (reference)	—
Standard PINN	0.0169	2.78 \times	1.00 \times (reference)
Pure NN	0.0201	3.31 \times	1.19 \times

The near-identical slopes of Standard PINN and Pure NN (ratio: 1.19 \times) suggest that soft-constraint physics integration does not qualitatively alter the extrapolation failure mechanism: both architectures ultimately rely on interpolation within the training manifold and diverge comparably once cathode pressure substantially exceeds the training range.

A.5.8 Per-Pressure Wilcoxon Results

Table S13 presents pairwise Wilcoxon signed-rank test results stratified by cathode pressure.

Note on 120 bar result. At 120 bar, the comparison between PR-Net and Standard PINN did not reach statistical significance ($p = 0.055$), representing the nearest extrapolation point at only 1.5 \times the training pressure range. This boundary finding is

Table S13 Per-pressure one-sided Wilcoxon signed-rank test results ($n = 8$ per pressure level; $\alpha = 0.05$, uncorrected).

Pressure	Pair	W	p	r	Significant?
120 bar	PR-Net < Standard PINN	6.0	0.055	-0.667	No
	PR-Net < Pure NN	1.0	0.008	-0.944	Yes
	Standard PINN < Pure NN	1.0	0.008	-0.944	Yes
160 bar	PR-Net < Standard PINN	1.0	0.008	-0.944	Yes
	PR-Net < Pure NN	0.0	0.004	-1.000	Yes
	Standard PINN < Pure NN	0.0	0.004	-1.000	Yes
200 bar	PR-Net < Standard PINN	2.0	0.012	-0.889	Yes
	PR-Net < Pure NN	0.0	0.004	-1.000	Yes
	Standard PINN < Pure NN	0.0	0.004	-1.000	Yes

consistent with soft-constraint methods partially retaining physical coherence at modest extrapolation distances, where the training manifold still provides some predictive coverage. This result does not affect the overall conclusions: all pairwise comparisons at 160 bar ($2.0\times$) and 200 bar ($2.5\times$) were statistically significant, and the global Friedman test and bootstrap confidence intervals (Sections A.5.4 and A.5.5) confirm PR-Net superiority across the full extrapolation range.

A.5.9 Statistical Power and Sample Size Justification

Post-hoc power analysis indicated:

- Achieved power: > 0.99 for detecting the observed effect sizes ($|r| \geq 0.87$) at $\alpha = 0.05$
- Sample size adequacy: $n = 24$ is sufficient for detecting large effect sizes at the corrected significance level

A.5.10 Aggregate Extrapolation Performance Across All Test Pressures

Table S14 presents the overall MAE and R^2 for each architecture across all extrapolation pressures.

Table S14 Aggregate predictive accuracy of the three architectures across the full extrapolation domain (120–200 bar; $n = 24$).

Model	MAE mean (%)	MAE s.d. (%)	R^2 (%)
PR-Net	0.375	0.250	98.52
Standard PINN	1.101	1.084	82.59
Pure NN	1.523	1.142	73.56

Figure S7 illustrates the architecture-specific absolute error distributions across the full extrapolation pressure range (120–200 bar), and Figure S8 presents bootstrap-derived confidence intervals quantifying the pairwise MAE reductions achieved by physics-constrained over less-constrained architectures.

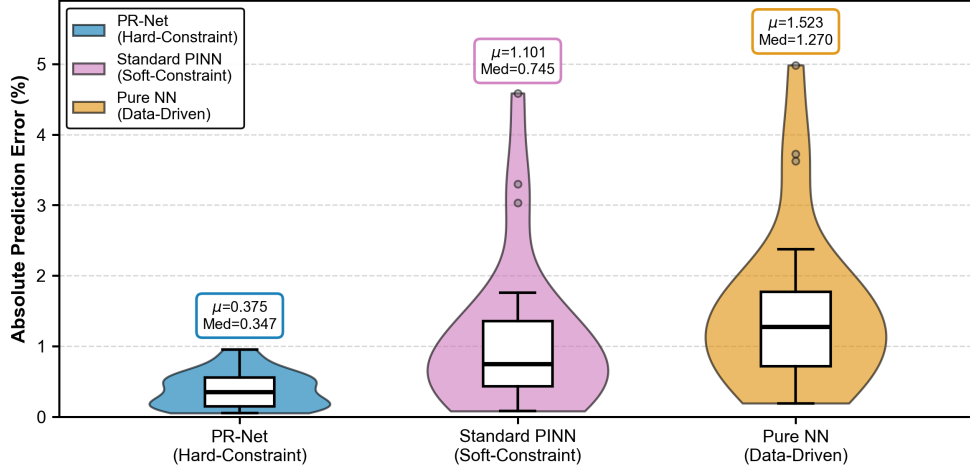


Fig. S7 Three-way comparison of absolute prediction error distributions across the full extrapolation pressure range (120–200 bar). Violin plots showing the distribution of absolute prediction errors for PR-Net (hard-constraint, blue), Standard PINN (soft-constraint, pink), and Pure NN (data-driven, orange) evaluated at cathode pressures of 120, 160, and 200 bar ($n = 24$ total test samples; Nafion 117, 25°C). Violin width represents the kernel density estimate of the error distribution. Overlaid box plots indicate the median (horizontal line), interquartile range (box), and $1.5 \times$ IQR whiskers; open circles denote outliers. Annotated values indicate the ensemble mean (μ) and median (Med) absolute error for each architecture. The compact, symmetric distribution of the PR-Net ($\mu = 0.375\%$, Med = 0.347%) contrasts markedly with the broad, right-skewed distributions of Standard PINN ($\mu = 1.101\%$) and Pure NN ($\mu = 1.523\%$), reflecting the stabilising effect of the hard-constraint physics backbone on prediction behaviour under high-pressure extrapolation conditions beyond the training domain. The Friedman omnibus test confirmed globally significant predictive performance differences among the three architectures ($\chi^2 = 35.58$, $p < 0.001$); pairwise Wilcoxon signed-rank tests with Holm–Bonferroni correction yielded large effect sizes for all comparisons ($|r| \geq 0.87$, $p_{\text{adj}} < 0.0001$; see Supplementary Table S9).

A.6 Supplementary Analysis: Economic Impact of PR-Net Implementation

The economic implications of accurate hydrogen crossover prediction via the PR-Net extend beyond operational safety. By enabling real-time monitoring and adaptive control, the proposed architecture directly contributes to significant OPEX and CAPEX reductions in industrial facilities.

Economic Sensitivity Analysis

The projected savings of \$200,000–1,500,000 annually for industrial facilities are derived from published cost benchmarks rather than direct model outputs (as detailed in Section 2.7 and Section 3 of the main text). Their realization requires integration with closed-loop control systems validated under sustained dynamic conditions. Key variables governing the magnitude of realized savings include:

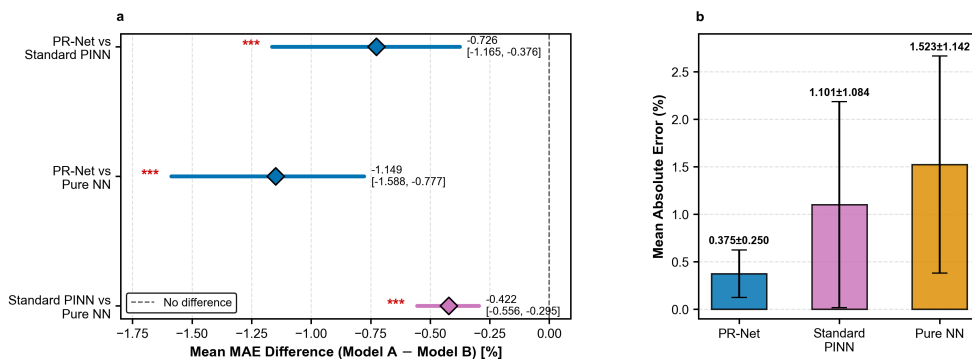


Fig. S8 Bootstrap confidence intervals for pairwise MAE differences and architecture-specific MAE reduction across the full extrapolation domain (120–200 bar). (a) Forest plot of 95% bootstrap confidence intervals (percentile method, 10,000 resamples) for mean absolute error (MAE) differences between paired model comparisons (Model A – Model B; $n = 24$; Nafion 117, 25°C). Diamond markers indicate the point estimate of the mean difference; horizontal lines span the 95% confidence interval. The vertical dashed line at zero denotes the null hypothesis of no difference. Red asterisks (***) indicate that the confidence interval excludes zero, confirming statistical significance. All three pairwise comparisons yield intervals entirely below zero, demonstrating that PR-Net achieves lower MAE than Standard PINN (-0.726% [95% CI: $-1.165, -0.376$]) and Pure NN (-1.149% [95% CI: $-1.588, -0.777$]), and that Standard PINN likewise outperforms Pure NN (-0.422% [95% CI: $-0.556, -0.295$]). (b) Bar chart of architecture-specific mean absolute error (mean \pm s.d.) across the full extrapolation pressure range. PR-Net achieves the lowest MAE ($0.375 \pm 0.250\%$), followed by Standard PINN ($1.101 \pm 1.084\%$) and Pure NN ($1.523 \pm 1.142\%$). The substantially larger standard deviations of Standard PINN and Pure NN reflect the pressure-amplified error instability of soft-constraint and data-driven architectures beyond the training domain, consistent with the right-skewed distributions shown in Supplementary Fig. S7.

- **Facility size and operating regime:** Savings scale with installed capacity and capacity factor; the present model is trained on static experimental observations and does not incorporate time-series aging trajectories.
- **Electricity cost:** Constitutes 60–80% of total hydrogen production expenses, making efficiency gains from adaptive current control (3–7%) the primary economic lever.
- **Stack replacement baseline:** Replacement costs of \$100,000–500,000 per cycle determine the financial impact of the 15–25% lifetime extension enabled by predictive maintenance.
- **Safety incident avoidance:** With 40% of hydrogen-related incidents attributed to undetected leaks, maintaining concentration below the 4 mol% explosive threshold through real-time monitoring is the critical non-financial driver.

Table S15 Economic Benefits Analysis: Projected annual savings by implementation scale

Benefit Category	Projected Value	Key Drivers	Source
Industrial Scale			
Annual savings	\$200,000–1,500,000/yr	Optimized maintenance scheduling and reduced unplanned downtime via real-time crossover monitoring	Main text, Sec 2.7
Stack lifetime extension	15–25% increase; \$100,000–500,000 deferred per replacement cycle	Continuous crossover monitoring enables targeted maintenance, reducing premature membrane failure	Main text, Sec 2.7
System efficiency gain	3–7% improvement	Adaptive current density control during renewable energy transients; electricity costs constitute 60–80% of production expenses	Main text, Sec 2.7
Safety			
Incident prevention	40% of H ₂ incidents caused by undetected leaks	Real-time monitoring maintains H ₂ concentration below 4 mol% explosive threshold	Main text, Sec 2.7
Total Industrial	\$200,000–1,500,000/yr	Combined maintenance, lifetime, and efficiency effects	Main text

Note: All projections are derived from published cost benchmarks, not direct model outputs. Realization requires integration with closed-loop control systems validated under sustained dynamic conditions.

A.6.1 Economic Sensitivity Analysis

The projected savings of \$200,000–1,500,000 annually for industrial facilities depend on several key variables:

- **Facility size:** 1–10 MW electrolyzer capacity
- **Electricity price:** \$0.05–0.10/kWh
- **Capacity factor:** 40–90%
- **Current baseline:** Conventional hydrogen production or no hydrogen use
- **Local incentives:** Tax credits, renewable energy certificates
- **Integration level:** Standalone vs. integrated with existing processes

A.7 Supplementary Methods

A.7.1 Hyperparameter Optimization

Systematic grid search was conducted to identify the optimal neural network architecture and training hyperparameters. The search space included:

- Learning rates: $[1 \times 10^{-4}, 1.5 \times 10^{-3}, 5 \times 10^{-3}, 1 \times 10^{-2}]$
- Hidden layer sizes: [32, 64, 128, 256]
- Number of hidden layers: [2, 3, 4, 5]
- Activation functions: [tanh, relu, silu]
- Regularization/Physics weights: $\lambda \in [0.1, 5.0]$ for PR-Net; $\beta \in [0.01, 0.9]$ for Standard PINN.

Optimal configuration: Both the proposed PR-Net and the baseline Standard PINN utilized the identical optimal architecture to ensure fair comparison: 3 hidden layers (128 neurons each), `tanh` activation, and Adam optimizer with a learning rate of 1.5×10^{-3} . For the PR-Net, the optimal residual regularization weight was fixed at $\lambda = 2.0$. For the Standard PINN, an adaptive linear decay schedule ($\beta : 0.7 \rightarrow 0.01$) yielded the most stable convergence.

A.7.2 Uncertainty Quantification Details

Deep ensemble uncertainty estimation for the extrapolation analysis followed this rigorous protocol:

1. **Training:** 100 independent models initialized with sequential random seeds (base seed 42 + model index, ranging from 42 to 141).
2. **Prediction:** Forward pass through all 100 ensemble members for each unseen test point.
3. **Statistics:**

- Mean point prediction: $\mu = \frac{1}{N} \sum_{i=1}^N \hat{y}_i$
- Epistemic uncertainty (ensemble variance): $\sigma^2 = \frac{1}{N-1} \sum_{i=1}^N (\hat{y}_i - \mu)^2$
- 95% Confidence Interval (CI): $\mu \pm 1.96\sigma$

A.7.3 Constitutive Physics Equations

Instead of imposing separate soft-loss terms for each intermediate variable, the PR-Net framework calculates the baseline hydrogen crossover concentration $\Phi_{H_2}^{\text{phys}}$ deterministically by solving a system of coupled constitutive equations. These equations account for material properties and transport phenomena as follows:

Temperature-Dependent Diffusivity

The self-diffusion coefficient of hydrogen in water ($D_{H_2,w}$) follows an Arrhenius relationship, with parameters fitted for the operating temperature range:

$$D_{H_2,w}(T) = 7.734 \times 10^{-6} \cdot \exp\left(-\frac{2225.4}{T}\right) \quad [\text{m}^2/\text{s}] \quad (\text{S1})$$

where T is the temperature in Kelvin.

Membrane Structural Parameters

Unlike simplified models that assume fixed structural parameters, our model dynamically calculates the water volume fraction ($\epsilon_{m,w}$) and tortuosity (τ_m) based on the membrane's specific water content (λ_m) and equivalent weight (EW):

$$\epsilon_{m,w} = \frac{\lambda_m V_w}{V_m + \lambda_m V_w} \quad (\text{S2})$$

$$\tau_m = (1 - 0.85(1 - \epsilon_{m,w}))^{-1} \quad (\text{S3})$$

Here, V_w is the molar volume of water and V_m is the molar volume of the dry membrane. This formulation accurately captures the swelling effect of the membrane on effective diffusivity ($D_{\text{eff}}^{H_2}$).

Compression Effects on LGDL

The model incorporates the impact of cell assembly pressure on the Liquid/Gas Diffusion Layer (LGDL). The compressed thickness (t_{LGDL}) and permeability (K_{LGDL}) are corrected using a cubic relation with porosity:

$$\phi_{\text{comp}} = 1 - \frac{t_{\text{initial}}}{t_{\text{comp}}} (1 - \phi_{\text{initial}}) \quad (\text{S4})$$

$$K_{\text{LGDL}} = K_{\text{initial}} \cdot \left(\frac{\phi_{\text{comp}}}{\phi_{\text{initial}}} \right)^3 \quad (\text{S5})$$

Physics Parameter Values

The key parameters used in the physics backbone are summarized below. Empirical mass transport parameters (α, β) are membrane-specific values optimized from experimental data via non-linear regression.

- **Constants:**

- Faraday constant: $F = 96,485 \text{ C mol}^{-1}$
- Molar volume of water: $V_w = 18.3 \text{ cm}^3 \text{ mol}^{-1}$
- Hydrogen molar mass: $M_{H_2} = 2.016 \times 10^{-3} \text{ kg mol}^{-1}$

- **Layer Properties (Default):**

- Anode CL thickness: $t_{CL,an} = 12.5 \mu\text{m}$
- Cathode CL thickness: $t_{CL,ca} = 5.0 \mu\text{m}$
- Ionomer volume fraction: $\epsilon_{io} = 0.15$
- LGDL Permeability: $K_{LGDL} = 2.0 \times 10^{-12} \text{ m}^2$
- CL Permeability: $K_{CL} = 2.6 \times 10^{-15} \text{ m}^2$

- **Model Parameters (Example for Nafion 117):**

- Convection parameter α : 5.52×10^{-3}
- Convection exponent β : Calculated via log-linear model ($a = 0.440, b = 0.0439$)

A.8 Supplementary Discussion

A.8.1 Comparison with Traditional Modeling Approaches

The proposed PR-Net architecture offers fundamental advantages over traditional modeling paradigms in electrochemical systems:

1. **Versus CFD & Mechanistic Models:** Achieves 5–6 orders of magnitude faster inference (4.45 ± 3.37 ms on a Raspberry Pi 4 versus minutes/hours for full CFD), enabling real-time edge deployment.
2. **Versus Pure Data-Driven ML:** Strictly ensures that thermodynamic conservation laws (e.g., Henry’s law) are satisfied, successfully preventing unphysical saturation and enabling robust extrapolation up to 200 bar.
3. **Versus Soft-Constraint PINNs:** Resolves the inherent gradient ”tug-of-war” between data fidelity and physical compliance, resulting in a 39-fold reduction in training variance and superior out-of-domain accuracy.

A.8.2 Limitations and Future Work

While the PR-Net demonstrates unprecedented extrapolation robustness and training stability, several areas warrant further investigation in future studies:

1. **Transient Degradation Dynamics:** The current model predicts steady-state crossover behaviors based on static membrane conditions. Future extensions should incorporate time-series aging trajectories and membrane thinning effects.
2. **Real-Gas Thermodynamics:** At extreme pressures approaching 200 bar, incorporating explicit fugacity corrections (e.g., Peng-Robinson equation of state) into the physical backbone could further refine the theoretical baseline.
3. **Platinum Interlayer Integration:** The current training dataset deliberately isolates non-interlayer membranes to maintain transport homogeneity. Incorporating Pt-doped membrane data represents a planned architectural extension.

A.8.3 Safety Considerations and System Integration

For industrial deployment, the PR-Net serves as the core computational engine within a broader safety monitoring architecture:

- **Primary Monitoring:** Provides millisecond-level, real-time H_2 concentration predictions across varying operational loads.
- **Fail-Safe Mechanism:** The structural decoupling allows the system to revert purely to the deterministic physics backbone ($\Phi_{H_2}^{\text{phys}}$) if the neural network residual exhibits anomalous epistemic uncertainty.
- **Regulatory Compliance:** The rapid inference time ensures that control systems can respond well within the $t_{90} \leq 30$ s response-time requirement specified by ISO 26142 for stationary hydrogen detection.